1   **Stepwise activation mechanism of the scramblase nhTMEM16 revealed by**

2   **cryo-EM**

3

4   Valeria Kalienkova[1], Vanessa Clerico Mosina[2], Laura Bryner[1], Gert T. Oostergetel[2], Raimund

5   Dutzler[1*] and Cristina Paulino[2*]

6   [1]Department of Biochemistry, University of Zürich, Winterthurer Str. 190, CH-8057 Zürich,

7   Switzerland

8   [2]Department of Structural Biology at the Groningen Biomolecular Sciences and Biotechnology

9   Institute, University of Groningen, Nijenborgh 7, 9747 AG Groningen, The Netherlands

10   [*]For correspondence: dutzler@bioc.uzh.ch (R.D.), c.paulino@rug.nl (C.P.)

1

11   **Abstract**

12   Scramblases catalyze the movement of lipids between both leaflets of a bilayer. Whereas the X-

13   ray structure of the protein nhTMEM16 has previously revealed the architecture of a Ca^{2+}-

14   dependent lipid scramblase, its regulation mechanism has remained elusive. Here, we have used

15   cryo-electron microscopy and functional assays to address this question. Ca^{2+}-bound and Ca^{2+}-free

16   conformations of nhTMEM16 in detergent and lipid nanodiscs illustrate the interactions with its

17   environment and they reveal the conformational changes underlying its activation. In this process,

18   Ca^{2+}-binding induces a stepwise transition of the catalytic subunit cavity, converting a closed

19   cavity that is shielded from the membrane in the absence of ligand, into a polar furrow that

20   becomes accessible to lipid headgroups in the Ca^{2+}-bound state. Additionally, our structures

21   demonstrate how nhTMEM16 distorts the membrane at both entrances of the subunit cavity,

22   thereby decreasing the energy barrier for lipid movement.

23

24

25   **Impact statement:** cryo-EM reveals the properties of distinct conformations occupied during

26   activation of the lipid scramblase nhTMEM16 and provides new insights into its interactions with

27   the lipid environment.

28 **Introduction**

29 The movement of lipids between both leaflets of a phospholipid bilayer, which is also referred to

30 as lipid flip-flop, is energetically unfavorable since it requires the transfer of the polar headgroup

31 from its aqueous environment across the hydrophobic core of the membrane (Kornberg and

32 McConnell, 1971). Consequently, spontaneous lipid flip-flop is rare and occurs at a time scale of

33 several hours. Whereas the sparsity of this event permits the maintenance of lipid asymmetry, there

34 are processes that require the rapid transbilayer movement of lipids (Bevers and Williamson, 2016;

35 Sanyal and Menon, 2009). Proteins that facilitate this movement by lowering the associated high

36 energy barrier are termed lipid scramblases (Pomorski and Menon, 2006; Williamson, 2015). Lipid

37 scramblases are generally non-selective and do not require the input of energy. They participate in

38 various cellular functions ranging from lipid signaling during blood coagulation and apoptosis to

39 the synthesis of membranes, cell division and exocytosis (Nagata et al., 2016; Whitlock and

40 Hartzell, 2016). First structural insight into lipid scrambling was provided from the X-ray structure

41 of the fungal protein from *Nectria haematococca*, termed nhTMEM16 (Brunner et al., 2014). This

42 protein is part of the TMEM16 family (Milenkovic et al., 2010), which encompasses calcium-

43 activated ion channels and lipid scramblases with a conserved molecular architecture (Brunner et

44 al., 2016; Caputo et al., 2008; Falzone et al., 2018; Schroeder et al., 2008; Suzuki et al., 2013;

45 Suzuki et al., 2010; Yang et al., 2008). As common for the family, nhTMEM16 is a homodimer

46 with subunits containing a cytoplasmic domain and a transmembrane unit composed of 10

47 membrane-spanning segments. The lipid permeation path is defined by a structural entity termed

48 the 'subunit cavity', which is located at the periphery of each subunit. In the X-ray structure, which

49 was obtained in the presence of Ca^{2+}, this site exposes a continuous polar cavity that spans the

50 entire membrane and that is of appropriate size to harbor a lipid headgroup (Brunner et al., 2014).

51   The 'subunit cavity' is believed to provide a pathway for the polar moieties of lipids across the

52   membrane, whereas the apolar acyl chains remain embedded in the hydrophobic core of the

53   membrane (Bethel and Grabe, 2016; Brunner et al., 2014; Jiang et al., 2017; Lee et al., 2018;

54   Malvezzi et al., 2018; Stansfeld et al., 2015). This process resembles a credit-card mechanism for

55   lipid scrambling, which was previously proposed based on theoretical considerations (Pomorski

56   and Menon, 2006). Although in this structure, Ca^{2+} ions were identified to bind to a conserved site

57   in the transmembrane domain, the mechanism of how Ca^{2+} activates the protein and how the

58   protein interacts with the surrounding lipids remained elusive. To gain insight into these questions,

59   we have determined structures of the protein in Ca^{2+}-bound and Ca^{2+}-free conformations by single

60   particle cryo-electron microscopy (cryo-EM), both in detergent and in a membrane environment

61   and we have characterized the effect of mutants on the activation process. Our data reveal two

62   essential features of the protein. They show how the protein deforms the membrane to lower the

63   energy barrier for lipid movement and to steer translocating lipids towards the subunit cavity.

64   Additionally, they define the conformational changes leading to the opening of the subunit cavity,

65   which is shielded from the membrane in a Ca^{2+}-free conformation, but exposes a hydrophilic

66   furrow for the permeation of lipids upon Ca^{2+} binding in a stepwise process involving coupled

67   ligand-dependent and ligand-independent steps.

68

69   **Results**

70   **Structural characterization of nhTMEM16 in detergent**

71   For our investigations of the ligand-induced activation mechanism of the lipid scramblase

72   nhTMEM16, we have recombinantly expressed the protein in the yeast *S. cerevisiae*, purified it in

73   the detergent n-Dodecyl β-D-maltoside (DDM) in the absence of Ca^{2+} and added Ca^{2+} during

4

74   sample preparation for structure determination and transport experiments. We have reconstituted

75   the purified protein into liposomes of different composition containing fluorescently labeled lipids

76   and characterized lipid transport using an assay that follows the irreversible decay of the

77   fluorescence upon addition of the membrane-impermeable reducing agent dithionite to the outside

78   of the liposomes (Brunner et al., 2014; Malvezzi et al., 2013; Ploier and Menon, 2016). In these

79   experiments we find a Ca^{2+}-dependent increase of transport but also a pronounced basal activity

80   of the protein in absence of Ca^{2+}, which was previously described as a hallmark of fungal

81   TMEM16 scramblases (Brunner et al., 2014; Malvezzi et al., 2013) (Figure 1-figure supplement

82   1). For the structural characterization of nhTMEM16, we have initially studied Ca^{2+}-bound and

83   Ca^{2+}-free samples in detergent by cryo-EM. By this approach, we have obtained two datasets of

84   high quality and of sufficient resolution (*i.e.* 3.6 Å for Ca^{2+}-bound and 3.7 Å for Ca^{2+}-free

85   conditions) for a detailed interpretation by an atomic model (Figure 1; Figure 1-figure supplements

86   2-4; Table 1). In the structure determined in the presence of Ca^{2+}, we find a conformation of the

87   protein, which closely resembles the X-ray structure with a root mean square deviation (RMSD)

88   of Cα atoms of 0.66 Å between the two structures (Figure 1D,E). The high similarity prevails

89   irrespective of the absence of crystal packing interactions and despite of the fact that the sample

90   used for cryo-EM was only briefly exposed to Ca^{2+} at a comparably low (*i.e.* 300 μM)

91   concentration, whereas for the X-ray structure, the protein was exposed to Ca^{2+} during purification

92   and crystallization at a 10-fold higher concentration (Brunner et al., 2014). Cryo-EM density at

93   the conserved Ca^{2+}-binding site, contained within each subunit of the homodimer, clearly indicates

94   the presence of two bound Ca^{2+} ions located at the position originally identified in the X-ray

95   structure (Figure 1F) (Brunner et al., 2014). Remarkably, we found a very similar structure of the

96   protein in the absence of Ca^{2+}, thus underlining the stability of this conformation in detergent

97   solution (Figure 1G,H). Although both datasets display equivalent conformations of the protein,

98   the structure determined in the absence of Ca^{2+} clearly shows an altered distribution of the divalent

99   ligand in its binding site, concomitant with a weaker density of the C-terminal part of α6 indicating

100 its increased mobility (Figure 1G,I; Figure1-figure supplement 3). The same region was previously

101 identified as key structural element in the Ca^{2+}-regulation of TMEM16A (Dang et al., 2017;

102 Paulino et al., 2017a; Peters et al., 2018). In the cryo-EM density, both strong peaks of the ligand

103 found in the Ca^{2+}-bound conformation are absent and instead replaced by weak residual density at

104 low contour located at the position of the lower Ca^{2+} ion (Figure 1F,I). Due to the presence of

105 millimolar amounts of EGTA in the buffer, the resulting free Ca^{2+}-concentration is in the pM

106 range, well below the estimated nM potency of the divalent cation (Figure 1-figure supplement 1).

107 Thus, whereas we do not want to exclude the possibility of Ca^{2+} binding at low occupancy, this

108 density might as well correspond to a bound Na^+ ion, which is present in the sample buffer at a

109 concentration of 150 mM (*i.e.* at a 10^{10} times higher concentration compared to Ca^{2+}). We think

110 that the stability of the open conformation displayed in the structures of the protein in detergent,

111 irrespectively of the presence of bound Ca^{2+}, does not reflect an intrinsic rigidity of the subunit

112 cavity. Instead, it is likely a consequence of experimental conditions, which stabilize the observed

113 conformation of the protein. This is in accordance with residual density from the headgroup of a

114 bound detergent molecule at the upper part of the lipid translocation path found in both datasets,

115 which might prevent subunit cavity closure (Figure 1-figure supplement 5). Interestingly, the

116 detergent molecule is interacting with Tyr 439, a residue that was shown to be essential for lipid

117 translocation in MD simulations and functional studies (Lee et al., 2018). The Ca^{2+}-free structure

118 in detergent thus likely displays a conformation that is responsible for the basal activity observed

6

119   for nhTMEM16 and other fungal scramblases (Figure 1-figure supplement 1) (Brunner et al., 2014;

120   Malvezzi et al., 2013). We expect this state to be less populated in a lipid bilayer.

121

122   **Structure of the Ca^{2+}-free state of nhTMEM16 in lipid nanodiscs**

123   The absence of conformational changes in the subunit cavity of nhTMEM16 in detergents

124   motivated us to study the structure of the protein in a lipid bilayer. For that purpose, we have

125   reconstituted nhTMEM16 into nanodiscs of different sizes using a lipid composition at which the

126   protein retains its lipid scrambling activity, although with considerably slower kinetics (Figure 1-

127   figure supplement 1C). In order to make sure that the scramblase is surrounded by a sufficiently

128   large membrane area, we assembled 2N2 scaffolding proteins with nhTMEM16 at three different

129   lipid to protein ratios (LPR) in the absence of Ca^{2+} and collected small datasets for all of them

130   (Figure 2-figure supplement 1). In all cases, the protein is located close to the center of an elliptic

131   disc with its long dimension oriented about parallel to the shortest side of the disc, a behavior that

132   is more pronounced in larger discs obtained at high lipid to protein ratios (Figure 2-figure

133   supplement 1). The orientation reflects a preference of lipids for locations distant from the subunit

134   cavity, which appears to deform the nanodisc. Since increasing the amount of lipids only caused

135   elongation of the nanodisc in one direction without a change in its diameter near the subunit cavity,

136   we proceeded with data collection on the sample with the lowest LPR of 145:1, which resulted in

137   a homogeneous assembly of approximately 165 x 140 Å in size (Figure 2-figure supplement 1A).

138   This approach was used to determine the structures of ligand-bound and ligand-free states of

139   nhTMEM16 in a membrane-like environment. The data is of excellent quality and provide an

140   unambiguous view of nhTMEM16 in different conformations (Figures 2 and 3; Figure 2-figure

141   supplements 2; Figure 3-figure supplements 1-2; Tables 1 and 2).

7

142   The differences between structures of nhTMEM16 determined in detergents and in a lipid

143   environment are most pronounced for the Ca^{2+}-free state determined at 3.8 Å resolution (Figure

144   2A,B,D; Figure 2-figure supplement 2). Whereas the structure in detergent displays a Ca^{2+}-free

145   conformation where the subunit cavity remains open to the membrane, the same region has

146   changed its accessibility in the nanodisc sample. Here, the movement of α4 leads to a shielding of

147   the cavity from the membrane core, resembling a conformation observed in the ion channel

148   TMEM16A (Figure 2E) (Dang et al., 2017; Paulino et al., 2017a; Paulino et al., 2017b). This

149   movement is accompanied by a conformational change of α6 as a consequence of the repulsion of

150   negatively charged residues in the empty Ca^{2+}-binding site (Figure 2B-D). Generally, the Ca^{2+}-

151   free state of nhTMEM16 in nanodiscs is very similar to equivalent structures of its close homologs

152   afTMEM16 (Falzone et al., 2019), TMEM16K (Bushell et al., 2018) and the more distantly related

153   scramblase TMEM16F (Alvadia et al., 2018) (Figure 2C,F and Figure 1-figure supplement 4), thus

154   underlining that all structures represent inactive conformations of the scramblase in the absence of

155   ligand.

156

157   **Structures of Ca^{2+}-bound states of nhTMEM16 in lipid nanodiscs**

158   Different from the data of the Ca^{2+}-free protein in nanodiscs, which comprises a single prevailing

159   state, the cryo-EM data obtained for the Ca^{2+}-bound samples in the same environment shows a

160   large heterogeneity along the 'subunit cavity'. This heterogeneity allows to sample the transition

161   of the lipid permeation path from the closed to the open state and emphasizes the intrinsic dynamics

162   of this region during activation (Figure 3; Figure 3-figure supplements 1 and 2; Table 2). A

163   classification of the data yielded several states with distinct conformations of the 'subunit cavity',

164   all of which exhibit well-resolved cryo-EM density for two Ca^{2+} ions and a rigid arrangement of

8

165   α6 in place to coordinate the divalent ions (Figure 3A-C; Figure 3-figure supplements 1 and 2).

166   About 50% of the particles define classes where α3 and α4 are poorly resolved, thus emphasizing

167   the high degree of flexibility in the region, which suggest that several states along the activation

168   process might be transient (classes 5 and 6, Figure 3-figure supplement 1C). By contrast, three

169   classes show well resolved distinct conformations. The 'open' class, at 3.6 Å resolution,

170   encompasses about 25% of the particles and strongly resembles the Ca^{2+}-bound open state obtained

171   in detergent, with a subunit cavity that is exposed to the membrane (Figure 3A; Figure 3-figure

172   supplements 1 and 2). In contrast, the 'Ca^{2+}-bound closed' class determined from 15% of particles

173   at 3.6 Å resolution, strongly resembles the 'Ca^{2+}-free closed' state obtained in nanodiscs, with a

174   subunit cavity that is shielded from the membrane, except that Ca^{2+} is bound and α-helix 6 is less

175   mobile (Figure 3C,G; Figure 3-figure supplements 1 and 2). The third distinct state at 3.7 Å

176   resolution encompasses 12% of all particles and shows an 'intermediate' conformation, where the

177   subunit cavity is still shielded from the membrane but where a potential aqueous pore surrounded

178   by α-helices of the subunit cavity has widened compared to the closed state (Figure 3B,E,F; Figure

179   3-figure supplements 1 and 2). The distribution of states, with a portion of nhTMEM16 residing

180   in potentially non-conductive conformations correlates with the lower activity of the protein in this

181   lipid composition (Figure 1-figure supplement 1C) and it emphasizes the equilibrium between

182   conformations of nhTMEM6 in the Ca^{2+}-bound state. Unassigned weak density in the subunit

183   cavity in the 'open' - but not in the 'closed' - conformation, hints at lipid molecules during the

184   transition between the leaflets (Figure 3-figure supplement 3). Strikingly, the strongest density is

185   located at an equivalent position as found for the potential DDM density in the cryo-EM maps of

186   nhTMEM6 in detergent (Figure 1-figure supplement 5).

187

9

188 **Conformational transitions**

189 The diversity of conformations of nhTMEM16 observed in various datasets and the presence of

190 different populations in the Ca^{2+}-bound sample in lipid nanodiscs suggest that our structures

191 represent distinct states along a stepwise activation process. Apart from a small rearrangements of

192 the cytosolic domain, the core of the protein is virtually identical in all structures and the largest

193 movements are observed in the vicinity of the subunit cavity (Figures 2D, 3D-G 4 and 5A and

194 Video 1). The Ca^{2+}-bound conformation in detergent and the 'open' class observed in the data of

195 Ca^{2+}-bound protein in nanodiscs, both show the widest opening of the subunit cavity and thus

196 likely depict a scrambling-competent state of the protein (Figure 4A). In this open state, α-helices

197 4 and 6 are separated from each other on their entire length framing the two opposite edges of a

198 semicircular polar furrow that is exposed to the lipid bilayer (Figure 4A). In this case, the

199 interaction of α3 with α10 of the adjacent subunit on the intracellular side appears to limit the

200 movement of α4, thus preventing a further widening of the cavity on the intracellular side (Figures

201 5A-C). On the opposite border of the subunit cavity, α6 is immobilized in its position by the bound

202 Ca^{2+} ions, which results in a tight interaction with α7 and α8 (Figure 5D). In the 'intermediate'

203 class found in the Ca^{2+}-bound sample in nanodiscs, we find marked conformational changes

204 compared to the 'open state'. The most pronounced differences are found for the α3-α4 pair. The

205 intracellular part of α3 (but not the α2-α3 loop contacting the helix Cα1 following α10) has

206 detached from its interaction with α10, leading to a concomitant movement of α4 at the same

207 region (Figure 5B). This movement has also affected the conformation of the extracellular part of

208 α4, which has rotated and approached α6, thereby forming initial contacts between both helices

209 (Figures 4B and 5C,D). The subunit cavity in this conformation is no longer exposed to the

210 membrane at its extracellular part and the structure likely represents an intermediate of the

10

211   scramblase towards activation (Figure 4B). This 'intermediate state' is remarkable in light of the

212   observed ion conduction of nhTMEM16 and other TMEM16 scramblases (Alvadia et al., 2018;

213   Lee et al., 2016; Suzuki et al., 2013; Yang et al., 2012; Yu et al., 2015), as it might harbor a

214   potential protein-enclosed aqueous pore located in region that is expanded compared to the 'closed

215   state' (Figure 5-figure supplement 1). The interactions between α4 and α6 on the extracellular side

216   further tighten in the 'closed' class found in the Ca^{2+}-bound sample in nanodiscs, thereby

217   constricting the aqueous pore observed in the 'intermediate state' (Figures 4C; Figure 5-figure

218   supplement 1). This conformation strongly resembles the Ca^{2+}-free 'closed' conformation

219   observed in nanodiscs, except that in the latter, the dissociation of the ligand from the protein has

220   allowed a relaxation of α6 leading to its detachment from α8 at the intracellular part of the helix

221   (Figures 4D and 5C,D). Although, unlike TMEM16A and TMEM16F, nhTMEM16 does not

222   contain a flexible glycine residue at the hinge, the movements of α6 upon Ca^{2+}-release occur at a

223   similar region (Alvadia et al., 2018; Paulino et al., 2017a) (Figure 2C-F and Figure 1-figure

224   supplement 4). In the transition from an 'open' to a 'closed state', α4 undergoes the largest changes

225   among all parts of nhTMEM16 with two prolines (Pro 332 and Pro 341) and a glycine (Gly 339)

226   serving as potential pivots for helix-rearrangements (Figure 5E and Video 1). Remarkably, both

227   prolines are conserved among fungal homologues and Pro 332 is also found in TMEM16K

228   (Bushell et al., 2018), the closest mammalian orthologue of nhTMEM16 (Figure 1-figure

229   supplement 4).

230

231   **Protein-induced distortion of the lipid environment**

232   A remarkable feature observed in the cryo-EM maps concerns the arrangement of detergent or

233   lipid molecules surrounding nhTMEM16, which allowed us to characterize the influence of the

11

234   protein on its environment. The observed distortions are found to a similar extent in all determined

235   structures, irrespective of the presence or absence of calcium in detergent or lipid nanodiscs and

236   can thus be considered a state-independent property of the protein. Neither detergent molecules

237   nor nanodisc lipids are uniformly distributed on the outside of nhTMEM16 (Figure 6 and Video

238   2). Instead, they adapt to the shape of the protein with distortions observed in the vicinity of the

239   shorter α-helices 1 and 8 at the extracellular side and at the gap between α-helices 4 and 6 at the

240   intracellular side (Figure 6). These distortions result in a marked deviation from the annular shape

241   of detergents molecules or lipids surrounding the protein found in most membrane proteins.

242   Remarkably, the resulting undulated distribution contains depressions in both the detergent and

243   lipid density close to the entrances of the subunit cavity (Figure 6 and Video 2). The arrangement

244   of the protein with its long dimension parallel to the short diameter of the oval-shaped nanodiscs

245   reflects the preferential location of lipids at sites distant from the subunit cavity (Figure 2-figure

246   supplement 1). The protein affects the distribution of lipids and the shape of the plane of the bilayer

247   in nanodiscs, which is slightly V-shaped and locally deviates from planarity at several regions

248   (Figure 6B,C). These pronounced depressions thin and distort the lipid structure at both ends of

249   the subunit cavity, thereby likely facilitating the entry of polar head-groups into the cavity and

250   lowering the barrier for lipid movement (Figure 6B).

251

252   Functional properties of mutants affecting the activation process

253   The distinct conformations of nhTMEM16 determined in this study hint at a sequential

254   mechanism, in which Ca^{2+}-dependent and independent steps are coupled to promote activation

255   similar to ligand-dependent ion channels. We have thus investigated the functional consequences

256   of mutations of residues of the Ca^{2+}-binding site and of the hinges for α4 movement with our

257   liposome-based lipid scrambling assay. The mutation D503A located on α7 concerns a residue of

258   the Ca^{2+}-binding site that does not change its position in different protein conformations and thus

259   should affect the initial ligand-binding step (Figure 7A). In this case, we find a Ca^{2+}-dependent

260   scrambling activity, although with strongly decreased potency of the ligand (Figures 7B,C). Next,

261   we investigated whether the mutation of two proline residues and a close-by glycine (Pro 332, Gly

262   339 and Pro 341), which form potential pivots during the rearrangement of α4 would affect lipid

263   scrambling (Figure 7A). Whereas we did not find any detectable effect in the mutant P341A, the

264   mutants G339A and P332A showed a strongly decreased activity both in the presence and absence

265   of Ca^{2+} (but no detectable change in the Ca^{2+}-potency of the protein, Figures 7D-F; Figure 7-figure

266   supplement 1). As the residues do not face the subunit cavity in the 'open state' and are unlikely

267   to interact with translocating lipids, we assume that these mutants alter the equilibrium between

268   active and inactive conformations thus emphasizing the role of conformational changes in α-helix

269   4 for nhTMEM16 activation.

270

271   **Discussion**

272   By combining data from cryo-electron microscopy and biochemical assays, our study has

273   addressed two important open questions concerning the function of a TMEM16 scramblase: it has

274   revealed the conformational changes that lead to the activation of the protein in response to Ca^{2+}

275   binding and it has shown how the protein interacts with the surrounding membrane to facilitate

276   lipid translocation. Structures in Ca^{2+}-free and bound states reveal distinct conformations of

277   nhTMEM16, which capture the catalytic subunit cavity of the scramblase at different levels of

278   exposure to the membrane during the activation process, representing a 'closed', at least one

279   'intermediate' and an 'open state'. As different protein conformations are observed in presence

280   and absence of its ligand, we propose a stepwise activation mechanism for TMEM16 scramblases,

281   where all states are at equilibrium (Figure 8; Figure 8-figure supplement 1). Here, the Ca^{2+}-free

282   conformation obtained in nanodiscs defines a non-conductive state of the protein, where the polar

283   subunit cavity is shielded from the membrane by tight interactions of α4 and α6 on the extracellular

284   part of the membrane (Figure 4D). The protein surface of the closed subunit cavity is hydrophobic

285   as expected for a membrane protein. This 'closed state' of nhTMEM16 resembles equivalent

286   structures obtained for the closely related lipid scramblases afTMEM16 (Falzone et al., 2019),

287   TMEM16K (Bushell et al., 2018), the more distantly related TMEM16F (Alvadia et al., 2018) and

288   the ion channel TMEM16A (Figure 2E,F) (Dang et al., 2017; Paulino et al., 2017a; Paulino et al.,

289   2017b), thus underlining that it is representative for an inactive conformation of both functional

290   branches of the family. In this conformation, the Ca^{2+}-binding site is empty, with the intracellular

291   part of α6 positioned apart from the remainder of the binding site to release the electrostatic strain

292   induced by the large negative net-charge in this region. Details of the conformation of α6 in the

293   absence of Ca^{2+} differ between the family members of known structure with the conformation in

294   nhTMEM16 being closer to the one observed for TMEM16F (Alvadia et al., 2018; Paulino et al.,

295   2017a).

296   During the activation process, Ca^{2+} binding provides interactions with residues on α6. The helix

297   rearranges into a locked state, as manifested in the well resolved cryo-EM density for its

298   intracellular half, which shields the binding site from the cytoplasm. This Ca^{2+}-induced movement

299   of α6 in nhTMEM16 is coupled to rearrangements in its interface with α4, potentially weakening

300   the interactions and resulting in a widening of the cavity. A cavity with a changed accessibility to

301   the membrane is displayed in a population of particles observed in the Ca^{2+}-bound nhTMEM16

302   structure in nanodiscs (Figure 4B). As the subunit cavity is not yet exposed to the membrane, the

303   'intermediate state' likely does not promote lipid scrambling. Instead, it might have opened a

304   protein-enclosed pore that could facilitate ion conduction (Figure 5-figure supplement 1), which

305   has been described as by-product of lipid scrambling in nhTMEM16 (Lee et al., 2016) and which

306   is a hallmark of the lipid scramblase TMEM16F (Alvadia et al., 2018; Yang et al., 2012; Yu et al.,

307   2015). Following the initial Ca^{2+}-induced conformational transition, the activation of lipid

308   scrambling requires a second step, which leads to a larger reorientation of α-helices 3 and 4 and a

309   subsequent opening of the polar subunit cavity to the membrane (Figures 3 and 4). This open state

310   is defined by the Ca^{2+}-bound structure of nhTMEM16 obtained in detergent and by one of the

311   classes observed in the Ca^{2+}-bound nanodisc dataset.

312   Thus, ion conduction and lipid-scrambling in nhTMEM16 and other TMEM16 scramblases might

313   be mediated by distinct conformations which are at equilibrium in a Ca^{2+}-bound protein (Figure 8;

314   Figure 8-figure supplement 1). This stepwise activation mechanism is in general accordance with

315   molecular dynamics simulations, which have started from the fully Ca^{2+}-bound open structure and

316   for which transitions leading to a partial closure of the subunit cavity have been observed in the

317   trajectories (Jiang et al., 2017; Lee et al., 2018). The basal scrambling activity of nhTMEM16 is

318   likely a consequence of the equilibrium between open, intermediate and closed conformations,

319   which is strongly shifted towards the closed state in the absence of Ca^{2+}. This is consistent with

320   the observation of a Ca^{2+}-free open state in detergent but not in nanodiscs, where the detergent

321   environment favors the equilibrium towards the open conformation (Figure 1H).

322   The cryo-EM structures of nhTMEM16 also reveal how the protein interacts with the surrounding

323   membrane to disturb its structure and consequently lower the energy barrier for lipid flip-flop, as

324   predicted from molecular dynamics simulations (Bethel and Grabe, 2016; Jiang et al., 2017; Lee

325   et al., 2018; Stansfeld et al., 2015). Our data reveal a pronounced distortion of the protein-

15

326   surrounding environment, which is stronger than observed for the ion channel TMEM16A (Paulino

327   et al., 2017b). This effect is preserved in all four datasets, irrespectively of the presence or absence

328   of ligand in detergent or nanodiscs, as their underlying structural features change little in the

329   different conformations. The distortion causes a deviation of the detergent or lipid molecules

330   surrounding nhTMEM16 from the annular structure observed in most membrane proteins (Figure

331   6 and Video 2). The resulting deformation of the membrane at the entrances to the subunit cavity

332   potentially serves to channel lipid headgroups through this hydrophilic furrow on their way across

333   the membrane.

334   In summary, our structures of nhTMEM16 have described how a calcium-activated lipid

335   scramblase is activated in a stepwise manner and how it bends the surrounding bilayer to promote

336   the transport of lipids between both leaflets of the membrane by a mechanism that is likely

337   conserved within the family.

338

339

340   **Materials and methods**

341   **Key resources table**

Reagent or Resource	Source	Identifier
Antibodies		
Mouse monoclonal Anti-c-Myc	Millipore Sigma	Cat#M4439; Clone#9E10
Peroxidase Affinipure goat anti-mouse IgG	Jackson Immunoresearch	Cat#115-035-146
Chemicals, Peptides, and Recombinant Proteins		
n-dodecyl-β-d-maltopyranoside (DDM), Solgrade	Anatrace	Cat#D310S
Water for molecular biology	Millipore	H20MB1006
Calcium nitrate tetrahydrate	Millipore Sigma	Cat#C4955
Sodium chloride	Millipore Sigma	Cat#71380
Magnesium chloride	Fluka	Cat#63065
HEPES	Millipore Sigma	Cat#H3375
Ethylene glycol-bis(2-aminoethylether)-N,N,N′,N′-tetraacetic acid	Millipore Sigma	Cat#03777
Ethylenediaminetetraacetic acid	Millipore Sigma	Cat#E6758

cOmplete, EDTA-free Protease Inhibitor Cocktail	Roche	Cat#5056489001
Biotin	Millipore Sigma	Cat#B4501
D-desthiobiotin	Millipore Sigma	Cat#D1411
Amicon Ultra-4 - 100 KDa cutoff	EMD Millipore	Cat#UFC8100
0.22 μm Ultrafree-MC Centrifugal Filter	EMD Millipore	Cat#UFC30GV
Glycerol	Millipore Sigma	Cat#G5516
1-palmitoyl-2-oleoyl-glycero-3-phosphocholine	Avanti Polar Lipids, Inc	Cat#850457C
1-palmitoyl-2-oleoyl-sn-glycero-3-phospho-(1'-rac-glycerol)	Avanti Polar Lipids, Inc	Cat#840457C
Diethyl ether	Millipore Sigma	Cat#296082
Bio-Beads SM-2 Adsorbents	Bio-Rad	Cat# 1523920
E. coli polar lipid extract	Avanti Polar Lipids, Inc	Cat#100600C
Egg PC, 95%	Avanti Polar Lipids, Inc	Cat#131601C
18:1-06:0 NBD-PE	Avanti Polar Lipids, Inc	Cat#810155C
Potassium chloride	Millipore Sigma	Cat#746436

CHAPS	Millipore Sigma	Cat#C3023
Sodium dithionite	Millipore Sigma	Cat#157953
Yeast nitrogen base without amino acids	Millipore Sigma	Cat#Y0626
Yeast Synthetic Drop-out Medium Supplements without uracil	Millipore Sigma	Cat#Y1501
D-Glucose	Applichem	Cat#A1422
Galactose	Millipore Sigma	Cat#G0625
Lithium acetate	Millipore Sigma	Cat#L4158
PEG3350	Millipore Sigma	Cat#88276
DNAse I	AppliChem	A3778-0500
HRV 3C protease	Raimund Dutzler laboratory	NA
Critical Commercial Assays		
Pierce Streptavidin Plus UltraLink Resin	Thermo Fisher Scientific	Cat#53117
Strep-Tactin® Superflow® high capacity	IBA Lifesciences	Cat#2-1208-010
Superdex 200 10/300 GL	GE Healthcare	Cat# 17-5175-01
Superose 6 10/300 GL	GE Healthcare	Cat#17-5172-01
Deposited Data		

Cryo-EM map and model of nhTMEM16 DDM +Ca^{2+}	This study	EMD-XXX, PDB ID XXXX
Cryo-EM map and model of nhTMEM16 DDM -Ca^{2+}	This study	EMD-XXX, PDB ID XXXX
Cryo-EM map and model of nhTMEM16 2N2 nanodiscs +Ca^{2+}	This study	EMD-XXX, PDB ID XXXX
Cryo-EM map and model of nhTMEM16 2N2 nanodiscs -Ca^{2+}	This study	EMD-XXX, PDB ID XXXX
Experimental Models: strains		
S. cerevisiae FGY217	David Drew laboratory	NA
Recombinant DNA		
nhTMEM16 open reading frame	GenScript	PubMed accession number XM_003045982
Yeast expression vector with N-terminal streptavidin binding peptide, Myc tag and 3C protease cleavage site	Raimund Dutzler laboratory	NA
Membrane scaffold protein (MSP) 2N2	Stephen Sligar laboratory	Addgene:Cat#29520
Software and Algorithms		

Online WEBMAXC calculator	Bers et al., 2010	http://maxchelator.stanford.edu/webmaxc/webmaxcS.htm
Focus 1.1.0	Biyani et al., 2017	https://focus.c-cina.unibas.ch/about.php
MotionCorr2 1.1.0	Zheng et al., 2017	http://msg.ucsf.edu/em/software/motioncor2.html
CTFFIND 4.1	Rohou et al., 2015	http://grigoriefflab.janelia.org/ctf
Relion v 2.1 and 3.0	Kimanius et al., 2016	https://www2.mrc-lmb.cam.ac.uk/relion/
Phenix 1.14	Adams et al., 2010	http:// http://phenix-online.org/
Coot 0.8.9.1	Emsley et al., 2004	https://www2.mrc-lmb.cam.ac.uk/personal/pemsley/coot/
Pymol 2.0	Schrodinger LLC	https://pymol.org/2/
Chimera 1.12	Pettersen et al., 2004	https://www.cgl.ucsf.edu/chimera/
ChimeraX 0.6	Goddard et al., 2018	https://www.rbvi.ucsf.edu/chimerax/

Other		
Whatman® Nuclepore™ Track-Etched Membranes diam. 19 mm, pore size 0.4 μm, polycarbonate	Millipore Sigma	Cat#WHA800282
HPL6	Maximator	NA
Fluoromax 4	Horiba	NA
300 mesh Au 1.2/1.3 cryo-EM grids	Quantifoil	Cat#N1-C14nAu30-01

342

343

344

Strains

346 Wild type *S. cerevisiae* FGY217 were grown either on YPD agar or in YPD liquid media

347 supplemented with 2% glucose at 30 °C. After the transformation with respective plasmids, the

348 cells were grown on yeast synthetic drop-out media without uracil with 2% glucose at 30 °C. For

349 protein expression, the cells were transferred into a selective media containing 0.1% glucose.

350

Construct preparation

352 The sequence encoding nhTMEM16 was cloned into a modified FX-cloning compatible (Geertsma

353 and Dutzler, 2011) pYES2 vector as a C-terminal fusion to streptavidin-binding peptide (SBP) and

354 Myc tags that were followed by an HRV 3C cleavage site. The mutations were introduced using a

355 QuickChange method (Zheng et al., 2004).

356

Protein expression and purification

All buffers were prepared using Ca^{2+}-free water for molecular biology (Millipore). Plasmids carrying the WT or mutant genes were transformed into the *S. cerevisiae* FGY217 strain as described (Gietz and Schiestl, 2007) using lithium acetate/single-stranded carrier DNA/polyethylene glycol method. The cells carrying the plasmid were grown at 30 °C in a yeast synthetic dropout media until the culture reached the OD_{600} of 0.8. Afterwards, the protein expression was initialized by adding 2% galactose and the temperature was decreased to 25 °C. The protein was expressed for 40 hours after induction. Cells were harvested at 7,200 *g* for 10 min and resuspended in buffer A (50 mM HEPES pH 7.6, 150 mM NaCl, 10 mM EGTA) containing 1 mM $MgCl_2$, DNAse and protease inhibitor cocktail tablets and lysed using a high pressure cell lyser HPL6 at 40 KPsi. Cell-debris was removed by centrifugation at 8,000 *g* for 30 min. Membranes were subsequently harvested by centrifugation with a 45 TI rotor (Beckmann) at 200,000 *g* for 1.5 hours, resuspended in buffer A containing 5% glycerol and flash-frozen in liquid N_2 and stored at -80 °C until further use. During purification, all steps were carried out at 4 °C or on ice. For purification, different amount of membrane vesicles were used depending on the purpose of the experiment: 30 g of membranes were used for sample preparation for cryo EM in detergent and in nanodiscs each, and 10 g of membranes for functional assays. Membranes were solubilized in buffer A containing 2% *n*-dodecyl-β-d-maltopyranoside (DDM) and 5% glycerol for 1.5 h. The insoluble fraction was removed by ultracentrifugation at 200,000 *g* for 30 min. The supernatant was applied to 4 ml of streptavidin Ultralink resin for 1.5 h, incubated under gentle agitation. The resin containing bound protein was subsequently washed with 50 column volumes (CV) of buffer B (10 mM HEPES pH 7.6, 150 mM NaCl, 5 mM EGTA, 0.03% DDM, 5% glycerol).

23

380   For sample preparation for cryo-EM in detergent, the purification tag was cleaved on the resin

381   with 2.4 mg of HRV 3C protease in buffer B containing 20 µg/ml of yeast polar lipids for 2 h. The

382   flow-through was collected, concentrated using 100 kDa cut-off centrifugal filter units at 700 g

383   and injected onto a Superdex 200 size-exclusion column equilibrated in buffer C (5 mM HEPES

384   pH 7.6, 150 mM NaCl, 2 mM EGTA, 0.03% DDM). Main peak fractions were pooled and

385   concentrated to 3.3 mg/ml as described above.

386   For sample preparation in lipid nanodiscs, membrane scaffold protein (MSP) 2N2 was expressed

387   and purified as described (Ritchie et al., 2009), except that the polyhistidine-tag was not removed.

388   Chloroform-solubilized lipids (POPC:POPG at a molar ratio of 7:3) were pooled, dried under a

389   nitrogen stream and washed twice with diethyl ether. The resulting lipid film was dried in a

390   desiccator overnight, and solubilized in 30 mM DDM at a final lipid concentration of 10 mM.

391   nhTMEM16 was purified as described above using the same amount of streptavidin resin, except

392   that the uncleaved fusion construct was eluted from the beads with buffer B containing 3 mM

393   biotin. Protein-containing fractions were pooled and concentrated as described above. Biotin was

394   removed from the sample via gel filtration on a Superdex 200 column. Purified protein was

395   assembled into 2N2 nanodiscs at three different molar ratios of protein:lipids:MSP (*i.e.* 2:725:10,

396   2:775:10, and 2:1100:10) as described (Ritchie et al., 2009). This procedure resulted in a five-fold

397   excess of empty nanodiscs, which prevented multiple incorporations of target proteins into a single

398   nanodisc. nhTMEM16 was mixed with detergent-solubilized lipids and incubated for 30 min on

399   ice. Subsequently, purified 2N2 was added to the sample, and the mixture was incubated for an

400   additional 30 min. Detergent was removed by incubating the sample overnight with SM-2 biobeads

401   (200 mg of beads/ml of the reaction) under constant rotation. From this point on, detergent was

402   excluded from all buffers. To separate the protein-containing from empty nanodiscs, the sample

24

403   was incubated with 1 ml of streptavidin resin for 1.5 hours. The resin was washed with 10 CV of

404   buffer B and assembled nanodiscs containing nhTMEM16 were eluted in buffer B containing 3

405   mM biotin. The purification tag was removed by incubation with 0.8 mg of HRV 3C protease for

406   2 hours. Cleaved samples were concentrated at 500 *g* using concentrators (Amicon) with a

407   molecular weight cut-off of 100 kDa and injected onto a Superose 6 column equilibrated in buffer

408   C. Analogously to the detergent sample, the main peak fractions were concentrated to around 2

409   mg/ml.

410   For reconstitution into proteoliposomes, nhTMEM16 was purified as described for detergent

411   samples used for cryo-EM with minor differences: lysate was incubated with 3 ml of streptactin

412   resin and eluted in buffer B containing 5 mM of d-desthiobiotin and the purification tag was not

413   removed.

414

415   **Reconstitution into the liposomes and scrambling assay**

416   Functional reconstitution was carried out essentially as described (Malvezzi et al., 2013). Lipids

417   for the reconstitution *(E. coli* polar extract and egg-PC at a ratio of 3:1 (w/w) was supplemented

418   with 0.5% (w/w) 18:1-06:0 NBD-PE) were pooled and dried as described above. The lipid film

419   was dissolved in assay buffer A (20 mM HEPES pH 7.5, 300 mM KCl, 2 mM EGTA) containing

420   35 mM CHAPS at a final lipid concentration of 20 mg/ml, aliquoted, flash-frozen and stored until

421   further use. Soy bean lipids extract with 20% cholesterol were prepared as described in Alvadia et

422   al, 2018. On the day of reconstitution, lipids were diluted to 4 mg/ml in assay buffer A and purified

423   protein was added to the lipid mixture at a lipid to protein ratio of 300:1 (w/w). As a control, an

424   equivalent volume of the gel filtration buffer was added to aliquots from the same batch of lipids

425   and treated the same way as the proteoliposomes sample, resulting in the assembly of empty

426   liposomes. Soy bean lipid mixture was destabilized with Triton X-100 as described in Alvadia et

427   al, 2018. The mixture was incubated for 15 min at room temperature (RT). Biobeads (15 mg of

428   beads/mg of lipids) were added 4 times (after 15 min, 30 min, 1 h and 12 h). After the second

429   addition of biobeads, the sample was transferred to 4 °C. The proteoliposomes were harvested by

430   centrifugation (150,000 g, 30 min, 4 °C), resuspended in assay buffer A containing desired

431   amounts of free Ca^{2+} (calculated with the WEBMAXC calculator) at a final concentration of 10

432   mg/ml in aliquots of 250 µl, flash-frozen and stored at -80 °C until further use. To characterize the

433   protein activity in the lipid mix used for the preparation of nanodisc samples, nhTMEM16 was

434   reconstituted into liposomes composed of 7 POPC:3 POPG (mol/mol) with 0.5 % 18:1-06:0 NBD-

435   PE. For conditions mimicking a eukaryotic membrane, the protein was reconstituted in soybean

436   polar lipids extract with 20% cholesterol (w/w) and 0.5% 18:1-06:0 NBD-PE. Each mutant was

437   purified and reconstituted independently three times on three different days (defined as distinct

438   biological replicate). To correct for differences in the reconstitution efficiency, WT was included

439   alongside with the mutants into each experiment, and reconstituted into the same batch of lipids

440   on the same day. Reconstitution of the WT into nanodisc lipids and soy bean lipids was performed

441   once.

442   On the day of the measurement, 250 µl aliquots of liposomes were frozen and thawed 3 times and

443   extruded 21 times through a 400 nm polycarbonate membrane using LipoFast extruder (Avestin).

444   Scrambling data was recorded on a Horiba Fluoromax spectrometer. For the measurement,

445   liposomes were diluted to 0.2 mg/ml in assay buffer B (80 mM HEPES pH 7.5, 300 mM KCl, 2

446   mM EGTA) containing corresponding amounts of free Ca^{2+}. odium dithionite was added after 60

447   sec to a final concentration of 30 mM and the fluorescence decay was recorded for additional 340

448   sec. Traces with deviations in fluorescence values of more than 0.03×10^6 counts per second within

26

449   the first 60 s of the measurement or displaying uncharacteristic spikes in fluorescence decay after

450   addition of dithionite were discarded. Each sample was measured three times (technical replicate).

451   Data were normalized as F/Fmax.

452   Under ideal conditions, all liposomes should be unilammelar and the lipid composition of the two

453   leaflets of the bilayer should be symmetric. Such scenario would result in a 50% fluorescence

454   decrease upon addition of dithionite to the outside of empty liposomes and a full decay of the

455   fluorescence in liposomes containing an active scramblase, which facilitates lipid flip-flop. In our

456   experiments, we observed fluorescence decays to plateau values ranging between 44–60% in

457   control liposomes and 10-20% in preparations of proteoliposomes containing nhTMEM16

458   constructs due to variabilities in liposome preparation. The incomplete decay is likely a

459   consequence of multilamellar liposomes and due to a fraction of liposomes not containing an active

460   scramblase in proteoliposome preparations. To account for differences in reconstitution efficiency,

461   all protein constructs that are directly compared to each other in our study and that are shown on

462   the same panel were reconstituted with the same batch of lipids on the same day and the analysis

463   is restricted to a phenotypical comparison of the decay kinetics. Reconstitution efficiency of

464   mutants as compared to wild type nhTMEM16 was estimated by Western blotting using a semi-

465   dry transfer protocol. Protein was transferred onto a PVDF membrane (Immobilon-P) and detected

466   using mouse anti-c-Myc antibody (Millipore Sigma) as a primary (1:5,000 dilution) and goat anti-

467   mouse coupled to a peroxidase (Jackson Immunoresearch) as a secondary antibody (1:10,000

468   dilution).

469

470   **Cryo-electron microscopy sample preparation and imaging**

27

471   2.5 μl of freshly purified protein at a concentration of 3.3 mg/ml when solubilized in DDMand at

472   about 2 mg/ml when reconstituted in nanodiscs were applied on holey-carbon cryo-EM grids

473   (Quantifoil Au R1.2/1.3, 200, 300 and 400 mesh), which were prior glow-discharged at 5 mA for

474   30 s. For datasets of Ca^{2+}-bound protein, samples (containing 2mM EGTA) were supplemented

475   with 2.3 mM $CaCl_2$ 30 minutes before freezing, resulting in a free calcium concentration of 300

476   μM. The pH change in response to the addition Ca^{2+} was monitored and found negligible. Grids

477   were blotted for 2–5 s in a Vitrobot (Mark IV, Thermo Fisher) at 10–15 °C and 100% humidity,

478   plunge-frozen in liquid ethane and stored in liquid nitrogen until further use. Cryo-EM data were

479   collected on a 200 keV Talos Arctica microscope (Thermo Fisher) at the University of Groningen

480   using a post-column energy filter (Gatan) in zero-loss mode, a 20 eV slit, a 100 μm objective

481   aperture, in an automated fashion using EPU software (Thermo Fisher) on a K2 summit detector

482   (Gatan) in counting mode. Cryo-EM images were acquired at a pixel size of 1.012 Å (calibrated

483   magnification of 49,407x), a defocus range from –0.5 to –2 μm, an exposure time of 9 s with a

484   sub-frame exposure time of 150 ms (60 frames), and a total electron exposure on the specimen of

485   about 52 electrons per $Å^2$. The best regions on the grid were screened and selected with an in-

486   house written script to calculate the ice thickness and data quality was monitored on-the-fly using

487   the software FOCUS (Biyani et al., 2017).

488

489   **Image Processing**

490   For the detergent dataset collected in presence of Ca^{2+}, the 2,521 dose-fractionated cryo-EM

491   images recorded (final pixel size 1.012 Å) were subjected to motion-correction and dose-weighting

492   of frames by MotionCor2 (Zheng et al., 2017). The CTF parameters were estimated on the movie

493   frames by ctffind4.1 (Rohou and Grigorieff, 2015). Images showing contamination, a defocus

494   above –0.5 or below –2 μm, or a poor CTF estimation were discarded. The resulting 2,023 images

495   were used for further analysis with the software package RELION2.1 (Kimanius et al., 2016).

496   Around 4,000 particles were initially manually picked from a subset of the dataset and classified

497   to create a reference for autopicking. The final round of autopicking on the whole dataset yielded

498   251,693 particles, which were extracted with a box size of 220 pixels and initial classification steps

499   were performed with two-fold binned data. False positives were removed in the first round of 2D

500   classification. Remaining particles were subjected to several rounds of 2D classification, resulting

501   in 174,901 particles that were further sorted in several rounds of 3D classification. A map created

502   from the X-ray structure of nhTMEM16 (PDBID: 4WIS) was low-pass filtered to 50 Å and used

503   as initial reference for the first round of 3D classification. The resulting best output class was used

504   as new reference in subsequent jobs in an iterative way. The best 3D classes, comprising 128,648

505   particles, were subjected to auto-refinement, yielding a map with a resolution of 4.3 Å. In the last

506   refinement iteration, a mask excluding the micelle was used and the refinement was continued

507   until convergence (focused refinement), which improved the resolution to 4.0 Å. The final map

508   was masked and sharpened during post-processing resulting in a resolution of 3.9 Å. Finally, the

509   newly available algorithms for CTF refinement and Bayesian polishing implemented in Relion3.0,

510   were applied to further improve the resolution (Zivanov et al., 2018). A final round of 3D

511   classification was performed, resulting in 120,086 particles that were subjected to refinement,

512   providing a mask generated from the final PDB model in the last iteration. The final map at 3.6 Å

513   resolution was sharpened using an isotropic B-factor of -126 $Å^2$. While a C1 symmetry was tested

514   and applied throughout image processing workflow, no indication of an asymmetry was identified.

515   Therefore, a C2-symmetry was imposed during the final 3D classification and auto-refinement.

516   Local resolution was estimated by RELION. All resolutions were estimated using the 0.143 cut-

517   off criterion (Rosenthal and Henderson, 2003) with gold-standard Fourier shell correlation (FSC)

518   between two independently refined half maps (Scheres and Chen, 2012). During post-processing,

519   the approach of high-resolution noise substitution was used to correct for convolution effects of

520   real-space masking on the FSC curve (Chen et al., 2013). The directional resolution anisotropy of

521   density maps was quantitatively evaluated using 3DFSC (Tan et al., 2017).

522   For the other datasets, a similar workflow for image processing was applied. In case of the

523   detergent dataset collected in absence of Ca^{2+}, a total of 570,203 particles were extracted with a

524   box size of 240 pixels from 2,947 images. Several rounds of 2D and 3D classification resulted in

525   a final number of 295,219 particles, which yielded a 3.9 Å map after refinement and post-

526   processing. CTF refinement and Bayesian polishing were applied, followed by a second round of

527   CTF refinement. One last round of 3D classification was performed, leading to a final pool of

528   238,070 particles which, after refinement and post processing, resulted in a map at 3.7 Å resolution.

529   For structure determination of nhTMEM16 in lipid nanodiscs, small datasets (around 1000 images)

530   recorded from samples reconstituted at different lipid to protein ratios (LPR) in absence of Ca^{2+}

531   during nanodisc assembly, identified the lowest LPR as optimal condition for large-scale data

532   collection. The dataset in nanodisc in absence of Ca^{2+} resulted in 1,379,187 auto-picked particles

533   from 6,465 images extracted with a box size of 240 pixels, which were reduced to 150,421 particles

534   after several rounds of 2D and 3D classification. CTF refinement and Bayesian polishing followed

535   by a final round of 3D classification was performed, resulting in a selection of 133,961 particles.

536   The final refinement and masking resulted in a 3.8 Å resolution map.

537   Finally, for the dataset in nanodiscs in the presence of Ca^{2+}, 2,440,110 particles were picked from

538   9,426 images and extracted with a box size of 240 pixels. Since the dataset displayed high

539   conformational heterogeneity, C1 symmetry was applied throughout the processing workflow.

540   After several rounds of 2D and 3D classification, the best classes (319,530 particles) were

30

541   combined and refined. The resulting map was used for CTF refinement in Relion3. Refined

542   particles were subjected to 3D refinement and the obtained map was used to generate a mask for

543   nanodisc signal subtraction. The resulting subtracted particles were used for another round of 3D

544   classification, yielding a subset of 279,609 particles. It was evident from the processing results

545   that the core of the protein was stable and displayed a single conformation, whereas α-helices 3

546   and 4 appeared to be mobile. To separate distinct conformational states, all the particles were

547   aligned using 3D refinement and subsequently subjected to a 3D classification without alignment,

548   using the angles obtained from the preceding refinement job. In one of the resulting classes, the

549   density corresponding to helices 3, 4 and 6 of one of the monomers was not defined, and these

550   particles (11,25%) were thus excluded from further processing. Of the remaining particles, 36,5%

551   are heterogeneous in the region corresponding to α-helices 3 and 4, 14,89% represent nhTMEM16

552   in a closed conformation of the subunit cavity, 11,91% in the intermediate, and two classes

553   (consisting of 15,64% and 9,81% particles respectively) display an open conformation. Each class

554   was subsequently initially refined applying C1 symmetry. Since no difference between the

555   conformations of individual subunits in the dimeric protein was detected, the refinement was

556   repeated with C2 symmetry imposed. The two open classes were merged and refined together.

557   Similar to other datasets, masks generated from PDB models were applied in the last iteration of

558   the refinement. After refinement and post-processing, the resulting resolutions were 3.57 Å for the

559   open class, 3.57 Å for the closed class and 3.68 Å for the intermediate class. We also attempted to

560   classify the heterogeneous class further, but could not improve the separation of the particles. To

561   generate the map of the open conformation containing the nanodisc signal, we reverted the

562   particles from the open class to their original non-subtracted equivalent, and refined them applying

563   C2 symmetry. This map was used to prepare Figure 3-supplement 3, Figure 6 and Video 2.

31

564

Model building refinement and validation

566 For the detergent dataset in the presence of Ca^{2+}, the X-ray structure of nhTMEM16 (PDBID:

567 4WIS) was used as a template. The model was manually edited in Coot (Emsley and Cowtan,

568 2004) prior to real-space refinement in Phenix imposing symmetry restraints between subunits

569 throughout refinement (Adams et al., 2010). The higher quality of the cryo-EM density of the

570 cytoplasmic domains compared to the X-ray density allowed for the identification of an incorrect

571 register at the N-terminus of the X-ray structure (PDBID: 4WIS) between residues 20-61. The

572 region comprising residues 15-61 was thus rebuilt. Another change compared to the X-ray

573 structure concerns the remodeled conformation of Lys 598. In several cases the cryo-EM density

574 allowed the interpretation of residues that were not defined in the X-ray structure. These concern

575 residues 130-140 at a loop connecting the cytoplasmic and the transmembrane domain, an extra

576 helical turn at the cytoplasmic side of α6 and residues 476-482 at the loop connecting α6 to α6'.

577 Since residues 690-698 appeared to be helical in the cryo-EM map, the region was rebuilt and it

578 was possible to add the missing residues 688-691. Several regions of the cryo-EM map displayed

579 weaker density compared to the X-ray structure, and hence the residues 416-418, 653-656 and

580 660-663 had to be removed from the model. This corrected nhTMEM16 structure (PDBID: 6QM5)

581 was used for refinement of the nhTMEM16 structure in DDM in the absence of Ca^{2+}, and for

582 model building and refinement of the Ca^{2+}-bound open and Ca^{2+}-bound closed structures in

583 nanodiscs. All models were edited manually in Coot, followed by real space refinement in Phenix.

584 The Ca^{2+}-free structure in DDM (PDBID: 6QM6) and the Ca^{2+}-bound open structure in nanodisc

585 (PDBID: 6QM9) closely resemble the Ca^{2+}-bound structure in DDM, displaying only minor

586 differences. Since the density corresponding to α6 is better resolved in the Ca^{2+}-bound open

32

587   structure in nanodisc, the helix was extended to Ser 471. The density corresponding to Cα2 of the

588   C-terminus (residues 664-684) was comparably weak in all three open structures and the helix was

589   thus fitted as a rigid body. For the Ca^{2+}-bound closed conformation (PDBID: 6QMB), major

590   changes were introduced for α3, α4 and to a lesser extent for α6. The densities of the loop

591   connecting α5' and α6 and of the cytosolic region of α6 were generally weaker and residues 417-

592   424 and 467-471 were thus not interpreted in this structure. Since the Ca^{2+}-bound closed map in

593   nanodisc displays the highest resolution and quality in the region encompassing α3 and α4, the

594   resulting model was used as a template for the interpretation of the Ca^{2+}-bound intermediate

595   (PDBID: 6QMA) and Ca^{2+}-free (PDBID: 6QM4) structures in nanodisc. In case of the Ca^{2+}-bound

596   intermediate structure, introduced changes are mostly confined to α4, where the extracellular part

597   of the α-helix undergoes a conformational transition towards opening of the subunit cavity. For

598   the Ca^{2+}-free structure in nanodisc, the residues 461-467 of α6 were not modelled due to its high

599   mobility. Figures were prepared using Pymol (The PyMOL Molecular Graphics System, Version

600   2.0 Schrödinger, LLC), Chimera (Pettersen et al., 2004) and ChimeraX (Goddard et al., 2018).

601

Acknowledgments

609

33

610 **Additional Information**

611 **Funding**

617

618 **Author contributions**

619 V.K. and L.B. purified proteins for cryo-EM and functional characterization. V.K. reconstituted

620 protein into nanodiscs and liposomes and carried out lipid transport experiments. V.K. and C.P.

621 prepared the samples for cryo-EM. V.K., V.C.M., G.T.O. and C.P. collected cryo-EM data. V.K.,

622 V.C.M and C.P. carried out image processing, model building and refinement. V.K., V.C.M, R.D.

623 and C.P. jointly planned experiments, analyzed the data and wrote the manuscript.

624

625 **Additional files**

626

627 **Data availability**

628 The three-dimensional cryo-EM density maps of calcium-free nhTMEM16 in detergent and

629 nanodiscs have been deposited in the Electron Microscopy Data Bank under accession numbers

630 EMD-4589 and EMD-4587, respectively. The maps of calcium-bound samples in detergent and

631 calcium-bound open, calcium-bound intermediate and calcium-bound closed in nanodiscs were

632   deposited under accession numbers EMD-4588, EMD-4592, EMD-4593 and EMD-4594,

633   respectively. The deposition includes the cryo-EM maps, both half-maps, the unmasked and

634   unsharpened refined maps and the mask used for final FSC calculation. Coordinates of all models

635   have been deposited in the Protein Data Bank. The accession numbers for calcium-bound and

636   calcium-free models in detergents are 6QM5 and 6QM6, respectively. The accession numbers for

637   calcium-bound open, calcium-bound intermediate, calcium-bound closed and calcium-free models

638   in nanodiscs are 6QM9, 6QMA, 6QMB and 6QM4, respectively.

639 **References**

640 Adams, P.D., P.V. Afonine, G. Bunkoczi, V.B. Chen, I.W. Davis, N. Echols, J.J. Headd, L.W.

641   Hung, G.J. Kapral, R.W. Grosse-Kunstleve, A.J. McCoy, N.W. Moriarty, R. Oeffner, R.J.

642   Read, D.C. Richardson, J.S. Richardson, T.C. Terwilliger, and P.H. Zwart. 2010. PHENIX:

643   a comprehensive Python-based system for macromolecular structure solution. *Acta*

644   *Crystallogr D Biol Crystallogr*. 66:213-221.

645 Alvadia, C., N.K. Lim, V. Clerico Mosina, G.T. Oostergetel, R. Dutzler, and C. Paulino. 2018.

646   Cryo-EM structures and functional characterization of the lipid scramblase TMEM16F.

647   *bioRxiv*.

648 Bethel, N.P., and M. Grabe. 2016. Atomistic insight into lipid translocation by a TMEM16

649   scramblase. *Proceedings of the National Academy of Sciences of the United States of*

650   *America*. 113:14049-14054.

651 Bevers, E.M., and P.L. Williamson. 2016. Getting to the Outer Leaflet: Physiology of

652   Phosphatidylserine Exposure at the Plasma Membrane. *Physiol Rev*. 96:605-645.

653 Biyani, N., R.D. Righetto, R. McLeod, D. Caujolle-Bert, D. Castano-Diez, K.N. Goldie, and H.

654   Stahlberg. 2017. Focus: The interface between data collection and data processing in cryo-

655   EM. *Journal of structural biology*. 198:124-133.

656 Brunner, J.D., N.K. Lim, S. Schenck, A. Duerst, and R. Dutzler. 2014. X-ray structure of a

657   calcium-activated TMEM16 lipid scramblase. *Nature*. 516:207-212.

658 Brunner, J.D., S. Schenck, and R. Dutzler. 2016. Structural basis for phospholipid scrambling in

659   the TMEM16 family. *Curr Opin Struct Biol*. 39:61-70.

660 Bushell, S.R., A.C.W. Pike, M.E. Falzone, N.J.G. Rorsman, C.M. Ta, R.A. Corey, T.D. Newport,

661   C.A. Shintre, A. Tessitore, A. Chu, Q. Wang, L. Shrestha, S. Mukhopadhyay, J.D. Love,

662   N.A. Burgess-Brown, R. Sitsapesan, P.J. Stansfeld, J.T. Huiskonen, P. Tommaro, A.

663   Accardi, and E.P. Carpenter. 2018. The structural basis of lipid scrambling and inactivation

664   in the endoplasmic reticulum scramblase TMEM16K. *bioRxiv*.

665 Caputo, A., E. Caci, L. Ferrera, N. Pedemonte, C. Barsanti, E. Sondo, U. Pfeffer, R. Ravazzolo,

666   O. Zegarra-Moran, and L.J. Galietta. 2008. TMEM16A, a membrane protein associated

667   with calcium-dependent chloride channel activity. *Science*. 322:590-594.

668 Chen, S., G. McMullan, A.R. Faruqi, G.N. Murshudov, J.M. Short, S.H. Scheres, and R.

669   Henderson. 2013. High-resolution noise substitution to measure overfitting and validate

670   resolution in 3D structure determination by single particle electron cryomicroscopy.

671   *Ultramicroscopy*. 135:24-35.

672 Dang, S., S. Feng, J. Tien, C.J. Peters, D. Bulkley, M. Lolicato, J. Zhao, K. Zuberbuhler, W. Ye,

673   L. Qi, T. Chen, C.S. Craik, Y.N. Jan, D.L. Minor, Jr., Y. Cheng, and L.Y. Jan. 2017. Cryo-

674   EM structures of the TMEM16A calcium-activated chloride channel. *Nature*. 552:426-429.

675 Emsley, P., and K. Cowtan. 2004. Coot: model-building tools for molecular graphics. *Acta*

676   *Crystallogr D Biol Crystallogr*. 60:2126-2132.

677 Falzone, M.E., M. Malvezzi, B.C. Lee, and A. Accardi. 2018. Known structures and unknown

678   mechanisms of TMEM16 scramblases and channels. *The Journal of general physiology*.

679 Falzone, M. E., J. Rheinberger, B.-C. Lee, T. Peyear, L. Sasset, A. Raczkowski, E. Eng, A. Di

680   Lorenzo, O.S. Andersen, C.M. Nimigean, and A. Accardi. 2019. Structural basis of Ca^{2+}-

681   dependent activation and lipid transport by a TMEM16 scramblase. *Elife* **8,** 213.

682 Geertsma, E.R., and R. Dutzler. 2011. A versatile and efficient high-throughput cloning tool for

683   structural biology. *Biochemistry*. 50:3272-3278.

684   Gietz, R.D., and R.H. Schiestl. 2007. High-efficiency yeast transformation using the LiAc/SS

685   carrier DNA/PEG method. *Nat Protoc*. 2:31-34.

686   Goddard, T.D., C.C. Huang, E.C. Meng, E.F. Pettersen, G.S. Couch, J.H. Morris, and T.E. Ferrin.

687   2018. UCSF ChimeraX: Meeting modern challenges in visualization and analysis. *Protein*

688   *Sci*. 27:14-25.

689   Jiang, T., K. Yu, H.C. Hartzell, and E. Tajkhorshid. 2017. Lipids and ions traverse the membrane

690   by the same physical pathway in the nhTMEM16 scramblase. *eLife*. 6.

691   Kimanius, D., B.O. Forsberg, S.H. Scheres, and E. Lindahl. 2016. Accelerated cryo-EM structure

692   determination with parallelisation using GPUs in RELION-2. *eLife*. 5.

693   Kornberg, R.D., and H.M. McConnell. 1971. Inside-outside transitions of phospholipids in vesicle

694   membranes. *Biochemistry*. 10:1111-1120.

695   Lee, B.C., G. Khelashvili, M. Falzone, A.K. Menon, H. Weinstein, and A. Accardi. 2018. Gating

696   mechanism of the extracellular entry to the lipid pathway in a TMEM16 scramblase. *Nat*

697   *Commun*. 9:3251.

698   Lee, B.C., A.K. Menon, and A. Accardi. 2016. The nhTMEM16 Scramblase Is Also a

699   Nonselective Ion Channel. *Biophysical journal*. 111:1919-1924.

700   Malvezzi, M., K.K. Andra, K. Pandey, B.C. Lee, M.E. Falzone, A. Brown, R. Iqbal, A.K. Menon,

701   and A. Accardi. 2018. Out-of-the-groove transport of lipids by TMEM16 and GPCR

702   scramblases. *Proceedings of the National Academy of Sciences of the United States of*

703   *America*.

704   Malvezzi, M., M. Chalat, R. Janjusevic, A. Picollo, H. Terashima, A.K. Menon, and A. Accardi.

705   2013. Ca2+-dependent phospholipid scrambling by a reconstituted TMEM16 ion channel.

706   *Nat Commun*. 4:2367.

707   Milenkovic, V.M., M. Brockmann, H. Stohr, B.H. Weber, and O. Strauss. 2010. Evolution and

708   functional divergence of the anoctamin family of membrane proteins. *BMC Evol Biol*.

709   10:319.

710   Nagata, S., J. Suzuki, K. Segawa, and T. Fujii. 2016. Exposure of phosphatidylserine on the cell

711   surface. *Cell Death Differ*. 23:952-961.

712   Paulino, C., V. Kalienkova, A.K.M. Lam, Y. Neldner, and R. Dutzler. 2017a. Activation

713   mechanism of the calcium-activated chloride channel TMEM16A revealed by cryo-EM.

714   *Nature*. 552:421-425.

715   Paulino, C., Y. Neldner, A.K. Lam, V. Kalienkova, J.D. Brunner, S. Schenck, and R. Dutzler.

716   2017b. Structural basis for anion conduction in the calcium-activated chloride channel

717   TMEM16A. *eLife*. 6.

718   Peters, C.J., J.M. Gilchrist, J. Tien, N.P. Bethel, L. Qi, T. Chen, L. Wang, Y.N. Jan, M. Grabe, and

719   L.Y. Jan. 2018. The Sixth Transmembrane Segment Is a Major Gating Component of the

720   TMEM16A Calcium-Activated Chloride Channel. *Neuron*. 97:1063-1077 e1064.

721   Pettersen, E.F., T.D. Goddard, C.C. Huang, G.S. Couch, D.M. Greenblatt, E.C. Meng, and T.E.

722   Ferrin. 2004. UCSF Chimera--a visualization system for exploratory research and analysis.

723   *J Comput Chem*. 25:1605-1612.

724   Ploier, B., and A.K. Menon. 2016. A Fluorescence-based Assay of Phospholipid Scramblase

725   Activity. *J Vis Exp*.

726   Pomorski, T., and A.K. Menon. 2006. Lipid flippases and their biological functions. *Cell Mol Life

727   Sci*. 63:2908-2921.

728   Ritchie, T.K., Y.V. Grinkova, T.H. Bayburt, I.G. Denisov, J.K. Zolnerciks, W.M. Atkins, and S.G.

729   Sligar. 2009. Chapter 11 - Reconstitution of membrane proteins in phospholipid bilayer

730   nanodiscs. *Methods in enzymology*. 464:211-231.

731   Rohou, A., and N. Grigorieff. 2015. CTFFIND4: Fast and accurate defocus estimation from

732   electron micrographs. *Journal of structural biology*. 192:216-221.

733   Rosenthal, P.B., and R. Henderson. 2003. Optimal determination of particle orientation, absolute

734   hand, and contrast loss in single-particle electron cryomicroscopy. *J Mol Biol*. 333:721-

735   745.

736   Sanyal, S., and A.K. Menon. 2009. Flipping lipids: why an' what's the reason for? *ACS Chem Biol*.

737   4:895-909.

738   Scheres, S.H., and S. Chen. 2012. Prevention of overfitting in cryo-EM structure determination.

739   *Nature methods*. 9:853-854.

740   Schroeder, B.C., T. Cheng, Y.N. Jan, and L.Y. Jan. 2008. Expression cloning of TMEM16A as a

741   calcium-activated chloride channel subunit. *Cell*. 134:1019-1029.

742   Smart, O.S., J.G. Neduvelil, X. Wang, B.A. Wallace, and M.S. Sansom. 1996. HOLE: a program

743   for the analysis of the pore dimensions of ion channel structural models. *Journal of*

744   *molecular graphics*. 14:354-360, 376.

745   Stansfeld, P.J., J.E. Goose, M. Caffrey, E.P. Carpenter, J.L. Parker, S. Newstead, and M.S.

746   Sansom. 2015. MemProtMD: Automated Insertion of Membrane Protein Structures into

747   Explicit Lipid Membranes. *Structure*. 23:1350-1361.

748   Suzuki, J., T. Fujii, T. Imao, K. Ishihara, H. Kuba, and S. Nagata. 2013. Calcium-dependent

749   phospholipid scramblase activity of TMEM16 protein family members. *J Biol Chem*.

750   288:13305-13316.

40

751   Suzuki, J., M. Umeda, P.J. Sims, and S. Nagata. 2010. Calcium-dependent phospholipid
752   scrambling by TMEM16F. *Nature*. 468:834-838.

753   Tan, Y.Z., P.R. Baldwin, J.H. Davis, J.R. Williamson, C.S. Potter, B. Carragher, and D. Lyumkis.
754   2017. Addressing preferred specimen orientation in single-particle cryo-EM through
755   tilting. *Nature methods*. 14:793-796.

756   Whitlock, J.M., and H.C. Hartzell. 2016. Anoctamins/TMEM16 Proteins: Chloride Channels
757   Flirting with Lipids and Extracellular Vesicles. *Annu Rev Physiol*.

758   Williamson, P. 2015. Phospholipid Scramblases. *Lipid Insights*. 8:41-44.

759   Yang, H., A. Kim, T. David, D. Palmer, T. Jin, J. Tien, F. Huang, T. Cheng, S.R. Coughlin, Y.N.
760   Jan, and L.Y. Jan. 2012. TMEM16F forms a Ca2+-activated cation channel required for
761   lipid scrambling in platelets during blood coagulation. *Cell*. 151:111-122.

762   Yang, Y.D., H. Cho, J.Y. Koo, M.H. Tak, Y. Cho, W.S. Shim, S.P. Park, J. Lee, B. Lee, B.M.
763   Kim, R. Raouf, Y.K. Shin, and U. Oh. 2008. TMEM16A confers receptor-activated
764   calcium-dependent chloride conductance. *Nature*. 455:1210-1215.

765   Yu, K., J.M. Whitlock, K. Lee, E.A. Ortlund, Y.Y. Cui, and H.C. Hartzell. 2015. Identification of
766   a lipid scrambling domain in ANO6/TMEM16F. *eLife*. 4:e06901.

767   Zheng, L., U. Baumann, and J.L. Reymond. 2004. An efficient one-step site-directed and site-
768   saturation mutagenesis protocol. *Nucleic Acids Res*. 32:e115.

769   Zheng, S.Q., E. Palovcak, J.P. Armache, K.A. Verba, Y. Cheng, and D.A. Agard. 2017.
770   MotionCor2: anisotropic correction of beam-induced motion for improved cryo-electron
771   microscopy. *Nature methods*. 14:331-332.

772   Zivanov, J., T. Nakane, B. Forsberg, D. Kimanius, W.J.H. Hagen, E. Lindahl, and S.H.W. Scheres.

773   2018. RELION-3: new tools for automated high-resolution cryo-EM structure
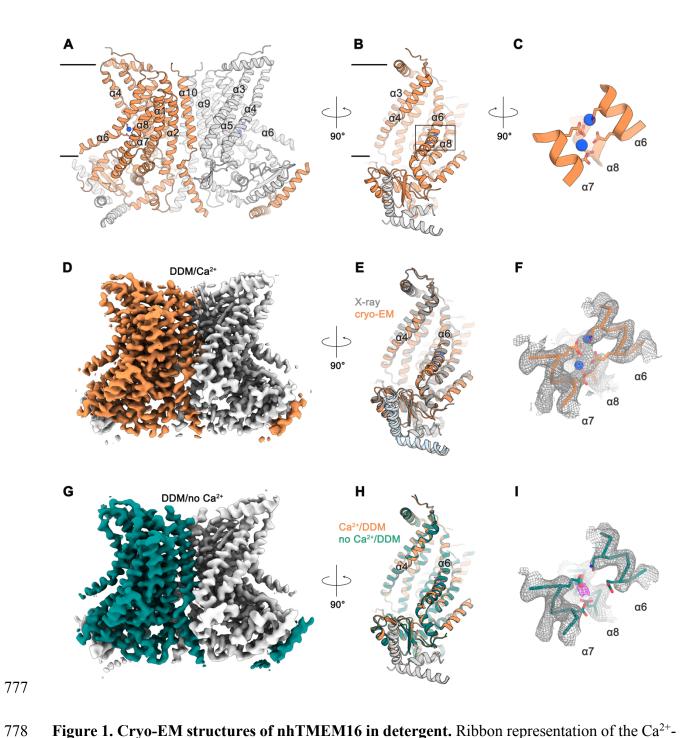
774   determination. *bioRxiv*.

775

776   **Figures**

777

778   **Figure 1. Cryo-EM structures of nhTMEM16 in detergent.** Ribbon representation of the Ca^{2+}-

779   bound cryo-EM structure of nhTMEM16 in detergent. The view is from within the membrane

780   perpendicular to the long dimension of the protein (**A**), towards the subunit cavity (**B**) and at the

43

781   Ca^{2+}-ion binding site (**C**). The membrane boundary is indicated. Subunits in the dimer are depicted

782   in orange and grey, respective transmembrane-helices are labelled and Ca^{2+}-ions are displayed as

783   blue spheres. Relative orientations are indicated and the location of the Ca^{2+}-binding site is

784   highlighted by a box in panel B. (**D**) Cryo-EM map of the nhTMEM16 dimer (orange and grey) in

785   DDM in presence of Ca^{2+} at 3.6 Å sharpened with a b-factor of -126 Å^2 and contoured at 6 σ. (**E**)

786   Ribbon representation of a superposition of the Ca^{2+}-bound structure in detergent determined by

787   cryo-EM (orange and grey) and the Ca^{2+}-bound X-ray structure (dark grey and light blue, PDBID:

788   4WIS) The view is as in panel B. (**F**) View of the Ca^{2+}-ion binding site of the Ca^{2+}-bound state of

789   nhTMEM16 in DDM. Ca^{2+}-ions are displayed as blue spheres. (**G**) Cryo-EM map of the

790   nhTMEM16 dimer (green and grey) in DDM in the absence of Ca^{2+} at 3.7 Å sharpened with a b-

791   factor of -147 Å^2 and contoured at 6 σ. (**H**) Ribbon representation of a superposition the Ca^{2+}-

792   bound (orange and grey) and the Ca^{2+}-free structure (green and grey) in detergent determined by

793   cryo-EM. The view is as in panel B. (**I**) View of the Ca^{2+}-binding site in the Ca^{2+}-free state of

794   nhTMEM16 in DDM. The location of weak residual density at the center of the Ca^{2+}-binding site

795   is indicated in magenta. F,I The respective cryo-EM densities are contoured at 7 σ and shown as

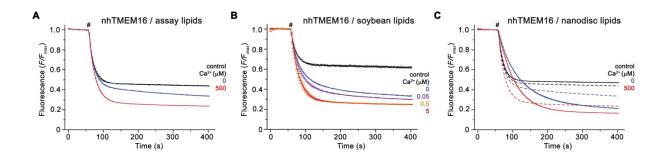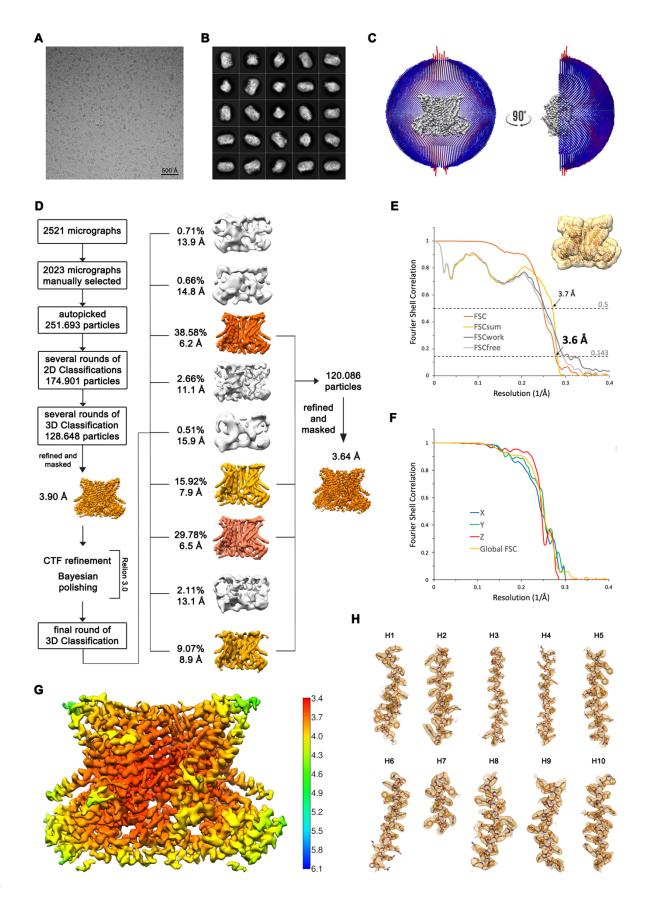796   mesh. The backbone is displayed as Cα-trace, selected side-chains as sticks.

797

798

799

Figure 1-figure supplement 1. Reconstitution of nhTMEM16 into liposomes. Ca^{2+}-dependence of scrambling activity of WT in liposomes of three different lipid compositions. Traces depict the fluorescence decrease of tail-labeled NBD-PE lipids after addition of dithionite (#) at different Ca^{2+} concentrations. Data show averages of three technical replicates for assay and nanodisc lipids, and of two for soybean lipids. Ca^{2+} concentrations (μM) are indicated. (**A**) Scrambling activity of nhTMEM16 reconstituted into liposomes composed of *E. coli* polar lipids, egg PC at a ratio of 3:1 (w/w) used for functional experiments. (**B**) Scrambling activity of nhTMEM16 reconstituted into liposomes composed of soybean polar lipids extract with 20% cholesterol (w/w). (**C**) Scrambling activity of nhTMEM16 reconstituted into liposomes composed of POPC/POPG at a molar ratio of 7:3 used for nanodisc assembly. Traces of *E. coli* polar lipids/egg PC-containing proteoliposomes (displayed in A) are shown as dashed lines for comparison.

811

812
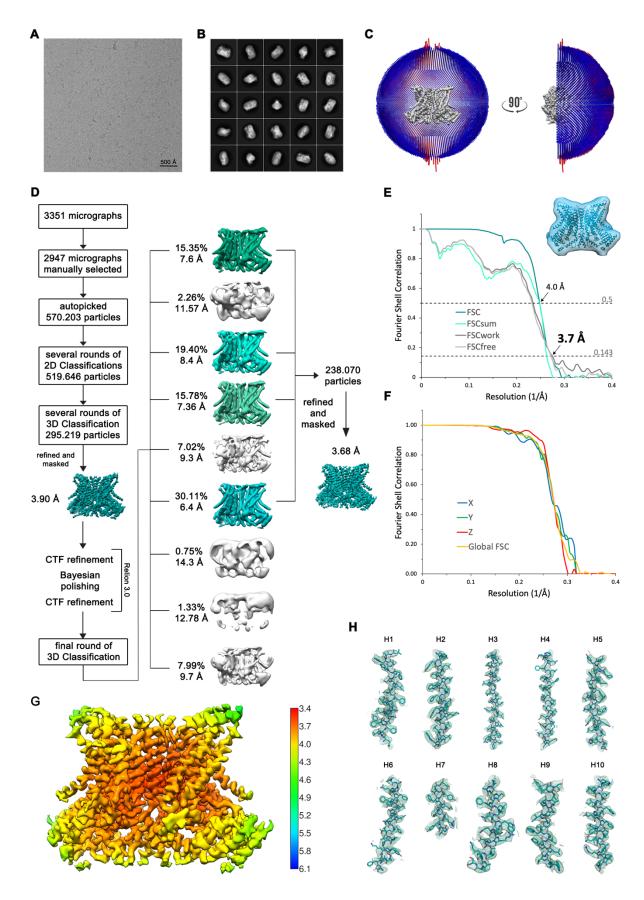
813   **Figure 1-figure supplement 2. Structure Determination of nhTMEM16 in DDM in complex**

814   **with Ca^{2+}.** (**A**) Representative cryo-EM image and (**B**) 2D-class averages of vitrified nhTMEM16

815   in a Ca^{2+}-bound state in detergent. (**C**) Angular distribution plot of particles included in the final

816   C2-symmetric 3D reconstruction. The number of particles with their respective orientation is

817   represented by length and color of the cylinders. (**D**) Image processing workflow. (**E**) FSC plot

818   used for resolution estimation and model validation. The gold-standard FSC plot between two

819   separately refined half-maps is shown in orange and indicates a final resolution of 3.6 Å. FSC

820   validation curves for FSCsum, FSCwork and FSCfree as described in the Methods are shown in

821   light yellow, dark grey and light grey, respectively. A thumbnail of the mask used for FSC

822   calculation overlaid on the atomic model is shown in the upper right corner and thresholds used

823   for FSCsum of 0.5 and for FSC of 0.143 are shown as dashed lines. (**F**) Anisotropy estimation plot

824   of the final map. The global FSC curve is represented in yellow. The directional FSCs along the

825   x, y and z axis displayed in blue, green and red, respectively, are indicative for an isotropic dataset.

826   (**G**) Final reconstruction map colored by local resolution as estimated by Relion, indicate regions

827   of higher resolution. (**H**) Sections of the cryo-EM density of the map superimposed on the refined

828   model. The model is shown as sticks and structural elements are labelled. The map was sharpened

829   with a b-factor of -126 Å^2 and contoured at 5 σ.

830

831

832 **Figure 1-figure supplement 3. Structure Determination of nhTMEM16 in DDM in absence**

833 **of Ca²⁺.** (**A**) Representative cryo-EM image and (**B**) 2D-class averages of vitrified nhTMEM16 in

834 a Ca²⁺-free state in detergent. (**C**) Angular distribution plot of particles included in the final C2-

835 symmetric 3D reconstruction. The number of particles with their respective orientation is

836 represented by length and color of the cylinders. (**D**) Image processing workflow. (**E**) FSC plot

837 used for resolution estimation and model validation. The gold-standard FSC plot between two

838 separately refined half-maps is shown in green and indicates a final resolution of 3.7 Å. FSC

839 validation curves for FSCsum, FSCwork and FSCfree as described in the Methods are shown in

840 cyan, dark grey and light grey, respectively. A thumbnail of the mask used for FSC calculation

841 overlaid on the atomic model is shown in the upper right corner and thresholds used for FSCsum

842 of 0.5 and for FSC of 0.143 are shown as dashed lines. (**F**) Anisotropy estimation plot of the final

843 map. The global FSC curve is represented in yellow. The directional FSCs along the x, y and z

844 axis displayed in blue, green and red, respectively, are indicative for an isotropic dataset. (**G**) Final

845 reconstruction map colored by local resolution as estimated by Relion, indicate regions of higher

846 resolution. (**H**) Sections of the cryo-EM density of the map superimposed on the refined model.

847 The model is shown as sticks and structural elements are labelled. The map was sharpened with a

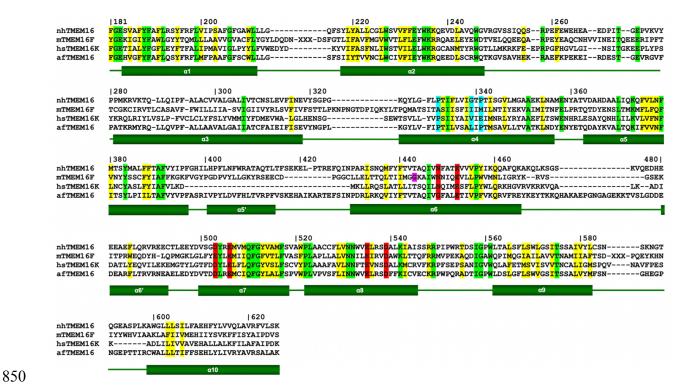848 Fig1_S4b-factor of −147 Å² and contoured at 5 σ.

849

Figure 1-figure supplement 4. Sequence alignment of selected TMEM16 scramblases. Protein sequences of the transmembrane domain of the fungal TMEM16 homologs from *Nectria haematococca* (nhTMEM16) and *Aspergillus fumigatus* (afTMEM16), murine TMEM16F and human TMEM16K were aligned based on their structure. Numbering and the boundaries of secondary structure elements (green rectangles for transmembrane-helices and green lines for loops) correspond to nhTMEM16. Residues highlighted in red constitute the Ca^{2+}-binding site; residues highlighted in blue act as potential pivot points for structural arrangements in α4; residue highlighted in purple indicates the flexible hinge region in TMEM16F responsible for the movements of α6 upon Ca^{2+} release.

861
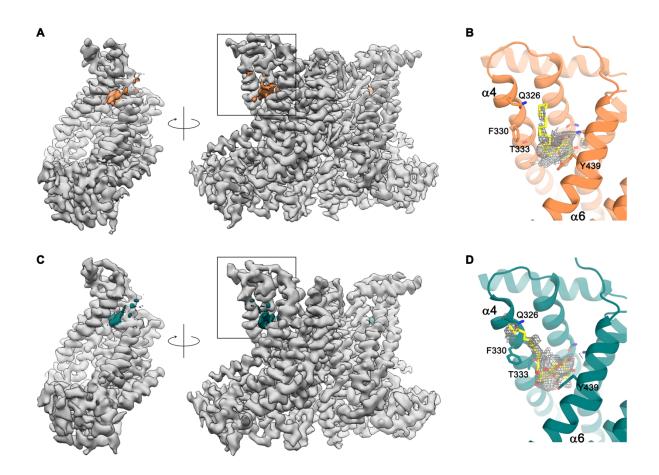
Figure 1-figure supplement 5. Detergent binding to the subunit cavity. (**A**) Cryo-EM map of the nhTMEM16 dimer in detergents in presence of Ca^{2+} (grey) in two orientations. Residual density in the subunit cavity highlighted in orange. (**B**) Ribbon representation of the subunit cavity of nhTMEM16 in detergents in presence of Ca^{2+}. Residual density (contoured at 5 σ) is shown as grey mesh. A DDM molecule (yellow) and selected sidechains are depicted as sticks. (**C**) Cryo-EM map of the nhTMEM16 dimer in detergents in absence of Ca^{2+} (grey) in two orientations. Residual density found in the subunit cavity is highlighted in green. (**D**) Ribbon representation of the subunit cavity of nhTMEM16 in detergents in absence of Ca^{2+} (green). Residual density (contoured at 5 σ) is shown as grey mesh. A DDM molecule (yellow) is depicted as sticks. The location of B,D is indicated by the box drawn on the right panel of A,C.
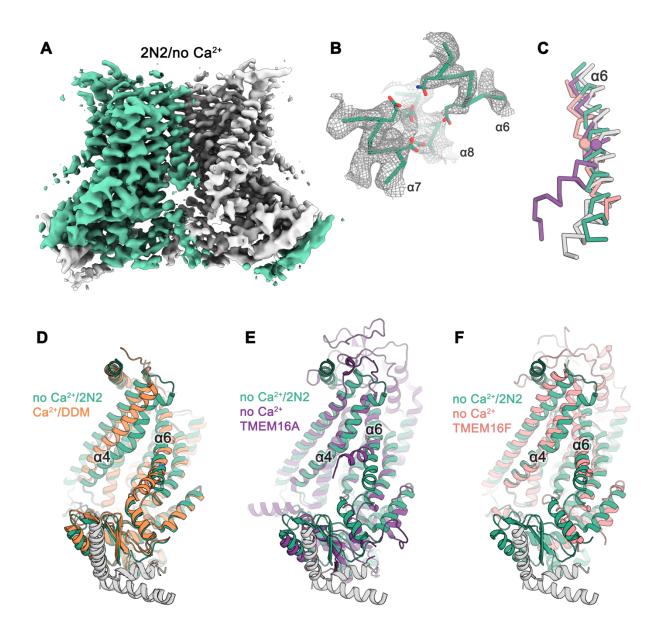
872

873

874

Figure 2. Cryo-EM structure of nhTMEM16 in nanodiscs in absence of Ca^{2+}. (**A**) Cryo-EM map of the nhTMEM16 dimer (light green and grey) in nanodiscs in absence of Ca^{2+} at 3.8 Å resolution. The map was sharpened with a b-factor of −150 Å^2 and is contoured at 5.6 σ. (**B**) View of the Ca^{2+}-binding site in the Ca^{2+}-free state of nhTMEM16 in nanodiscs. The cryo-EM density

880   shown as mesh is contoured at 6 σ, the backbone is displayed as Cα-trace and selected side-chains

881   as sticks. (**C**) Cα-traces of α6 from a superposition of Ca^{2+}-free structures of nhTMEM16 in

882   nanodiscs (green), TMEM16A (violet, PDBID: 5OYG) and TMEM16F (red) and of the Ca^{2+}-

883   bound structure of nhTMEM16 in DDM (grey). The spheres indicate the position of the flexible

884   glycine residue in TMEM16A and TMEM16F, which acts as a hinge for conformational changes.

885   (**D-F**) Ribbon representation of superpositions of the Ca^{2+}-free structure in nanodiscs (light green

886   and grey) and the Ca^{2+}-bound structure in DDM (**D**, orange and grey), the Ca^{2+}-free structure of

887   TMEM16A (**E**, violet, PDBID: 5OYG), the Ca^{2+}-free structure of TMEM16F (**F**, red). Selected

888   α-helices are labeled, the views are as in Figure 1.
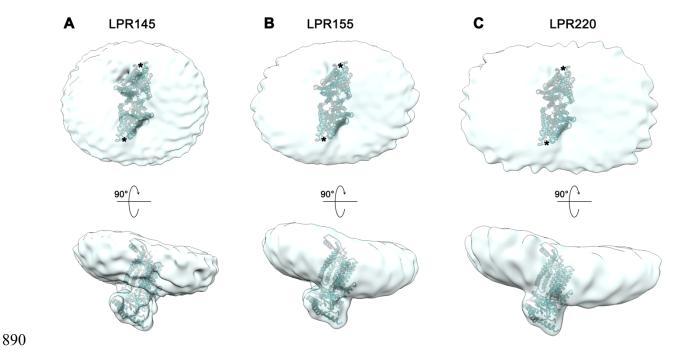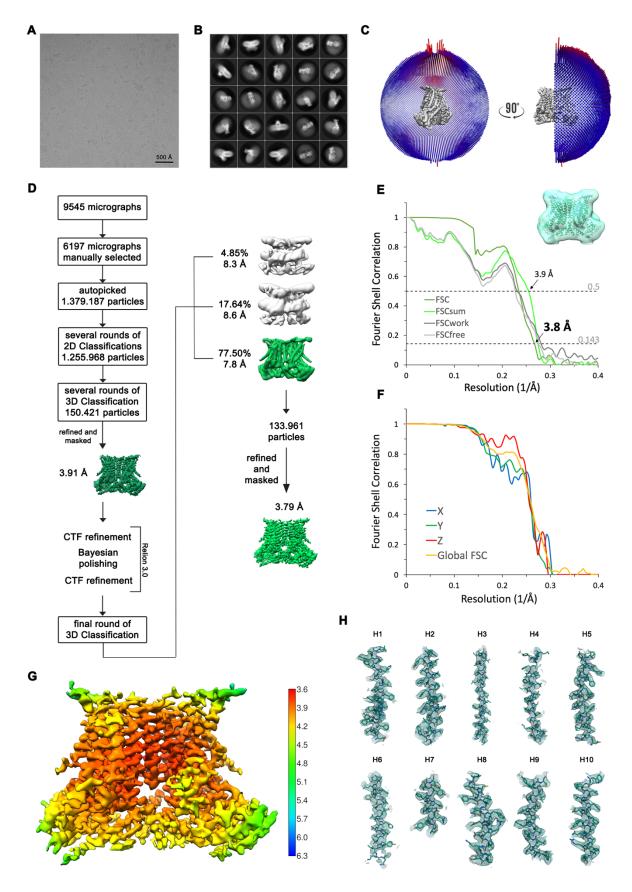
889

890

891   **Figure 2-figure supplement 1. Reconstitution of nhTMEM16 into nanodiscs.** Shape of

892   nhTMEM16 particles reconstituted into nanodiscs at different protein to lipid ratios (LPR,

893   mol/mol) in the absence of Ca^{2+}: (**A**), LPR 145, (**B**), LPR 155 and(**C**), LPR 220. Refined and

53

894   unmasked cryo-EM density maps were low-pass filtered to 10 Å and are shown from the

895   extracellular side (upper panel, subunit cavity indicated by *) and from the side with a view

896   towards the subunit cavity (lower panel). A model of nhTMEM16 fitted into the density is

897   displayed as ribbon.

898

899

900

901 **Figure 2-figure supplement 2. Structure Determination of nhTMEM16 in the absence of Ca^{2+}**

902 **in nanodiscs.** (**A**) Representative cryo-EM image and (**B**) 2D-class averages of vitrified

903 nhTMEM16 in a Ca^{2+}-free state in lipid nanodiscs. (**C**) Angular distribution plot of particles

904 included in the final C2-symmetric 3D reconstruction. The number of particles with their

905 respective orientation is represented by length and color of the cylinders. (**D**) Image processing

906 workflow. (**E**) FSC plot used for resolution estimation and model validation. The gold-standard

907 FSC plot between two separately refined half-maps is shown in green and indicates a final

908 resolution of 3.8 Å. FSC validation curves for FSCsum, FSCwork and FSCfree as described in the

909 Methods are shown in light green, dark grey and light grey, respectively. A thumbnail of the mask

910 used for FSC calculation overlaid on the atomic model is shown in the upper right corner and

911 thresholds used for FSCsum of 0.5 and for FSC of 0.143 are shown as dashed lines. (**F**) Anisotropy

912 estimation plot of the final map. The global FSC curve is represented in yellow. The directional

913 FSCs along the x, y and z axis displayed in blue, green and red, respectively, are indicative for an

914 isotropic dataset. (**G**) Final reconstruction map colored by local resolution as estimated by Relion,

915 indicate regions of higher resolution. (**H**) Sections of the cryo-EM density of the map

916 superimposed on the refined model. The model is shown as sticks and structural elements are

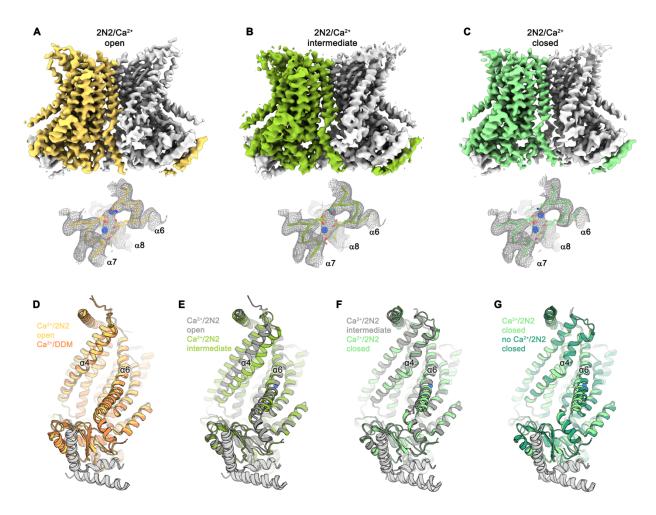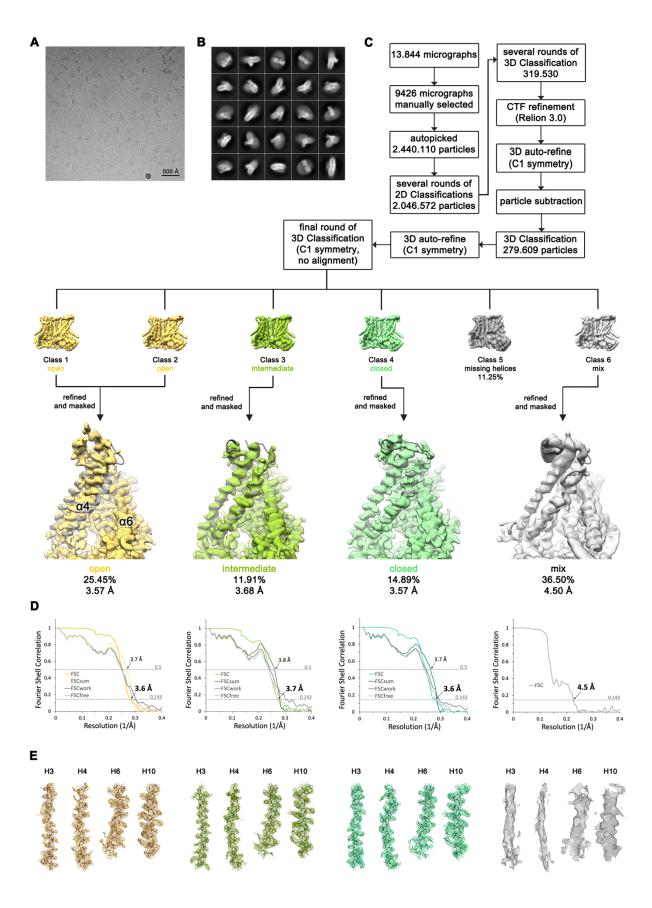917 labelled. The map was sharpened with a b-factor of -150 Å^2 and contoured at 5 σ.

918

919

Figure 3. Cryo-EM structures of nhTMEM16 in nanodiscs in presence of Ca^{2+}. (**A**) Cryo-EM map of the nhTMEM16 dimer in the Ca^{2+}-bound 'open' state (yellow and grey) in nanodiscs at 3.6 Å sharpened with a b-factor of -114 Å^2 and contoured at 6.5 σ (upper panel). Close-up of the Ca^{2+}-binding site with two bound Ca^{2+}-ions displayed as blue spheres (lower panel). Cryo-EM density contoured at 7 σ is shown as grey mesh, the backbone is displayed as yellow Cα-trace, selected side-chains as sticks. (**B**) Cryo-EM map of the nhTMEM16 dimer in the Ca^{2+}-bound 'intermediate' state (yellow-green and grey) in nanodiscs at 3.7 Å sharpened with a b-factor of $-$96 Å^2 and contoured at 4.9 σ (upper panel). Close-up of the Ca^{2+}-binding site with two bound Ca^{2+}-ions displayed as blue spheres (lower panel). Cryo-EM density contoured at 7 σ is shown as grey mesh, the backbone is displayed as light green Cα-trace, selected side-chains as sticks. (**C**) Cryo-

57

930   EM map of the nhTMEM16 dimer in the 'Ca^{2+}-bound closed state (green and grey) in nanodiscs

931   at 3.6 Å sharpened with a b-factor of –96 Å^2 and contoured at 6.5 σ (upper panel). Close-up of the

932   Ca^{2+}-binding site with two bound Ca^{2+}-ions displayed as blue spheres (lower panel). Cryo-EM

933   density contoured at 7 σ is shown as grey mesh, the backbone is displayed as light green Cα-trace,

934   selected side-chains as sticks. (**D-G**) Ribbon representation of superpositions with Ca^{2+}-bound

935   structures of nhTMEM16 in nanodiscs: (**D**) Ca^{2+}-bound open structure in nanodiscs and Ca^{2+}-

936   bound structure in DDM; (**E**) Ca^{2+}-bound open structure in nanodiscs and Ca^{2+}-bound intermediate

937   structure in nanodiscs; (**F**) Ca^{2+}-bound intermediate structure in nanodiscs and Ca^{2+}-bound closed

938   structure in nanodiscs; (**G**) Ca^{2+}-bound closed structure in nanodiscs and Ca^{2+}-free structure in

939   nanodiscs. Selected helices are labeled and views are as in Figure 1.

940

941

943 **Figure 3-figure supplement 1. Structure Determination of nhTMEM16 in complex with Ca^{2+}**

944 **in nanodiscs.** (**A**) Representative cryo-EM image and (**B**) 2D-class averages of vitrified

945 nhTMEM16 in a Ca^{2+}-bound state in lipid nanodiscs. (**C**) Image processing workflow. The final

946 set of subtracted particles was subjected to a final round of 3D classification disclosing a

947 conformational heterogeneity at the subunit cavity, with classes resembling a well-resolved open,

948 intermediate and closed state of the subunit cavity. Other classes displayed a poorly resolved

949 density for α3 and α4 that likely represents an average of several transition states. Close-up of the

950 subunit cavity show the intermediate model (grey) superimposed on the cryo-EM maps of the

951 respective classes. View as in Figure 3C-F. (**D**) FSC plot used for resolution estimation and model

952 validation for each state. The gold-standard FSC plot between two separately refined half-maps is

953 shown in yellow. FSC validation curves for FSCsum, FSCwork and FSCfree as described in the

954 Methods are shown in light yellow, dark grey and light grey, respectively. Thresholds used for

955 FSCsum of 0.5 and for FSC of 0.143 are shown as dashed lines. (**E**) Sections of the cryo-EM

956 density of the maps superimposed on the corresponding refined models. The models are shown as

957 sticks and structural elements are labelled. The maps were contoured at 4.5 σ.
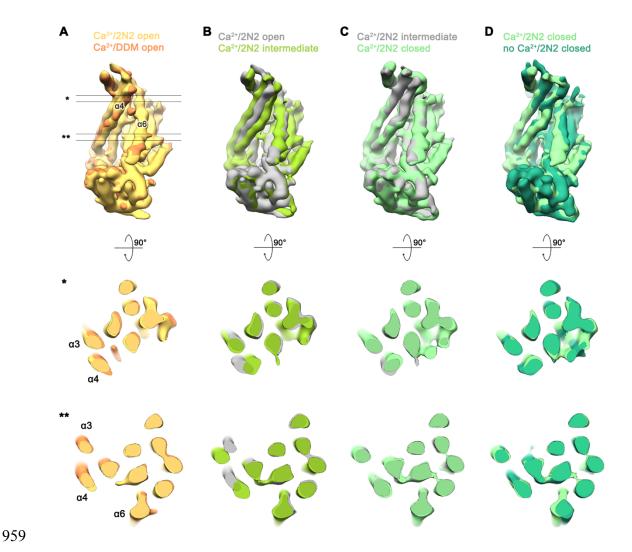
958

959

Figure 3-figure supplement 2. Conformational heterogeneity in the Ca^{2+}-bound data of nhTMEM16 in nanodiscs. (A-D) Superpositions of the refined and unmasked cryo-EM maps of Ca^{2+}-bound structures of nhTMEM16 in nanodiscs, low-pass filtered at 6 Å. (**A**) Superposition of the Ca^{2+}-bound open structure in nanodiscs and the Ca^{2+}-bound structure in DDM; (**B**) the Ca^{2+}-bound open structure in nanodiscs and the Ca^{2+}-bound intermediate structure in nanodiscs; (**C**) the Ca^{2+}-bound intermediate structure in nanodiscs and the Ca^{2+}-bound closed structure in nanodiscs; (**D**) the Ca^{2+}-bound closed structure in nanodiscs and the Ca^{2+}-free structure in nanodiscs. A-D, selected helices are labeled, view of upper panel is as in Figure 3C-F. Middle and lower panel

61

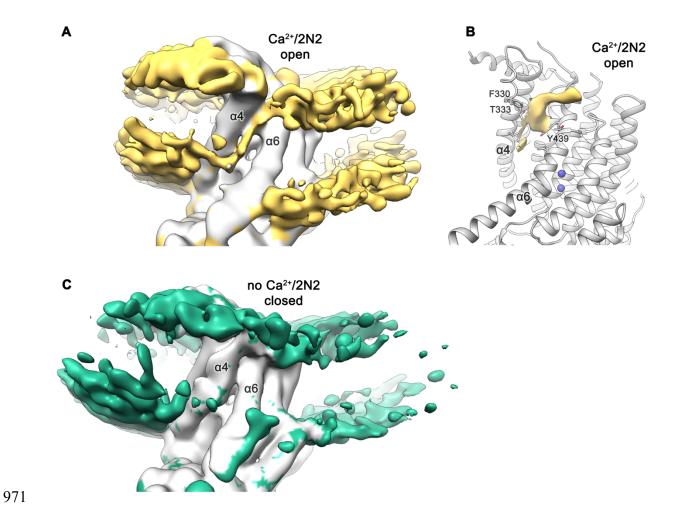968   show a cross-section through the superposition at the indicated positions indicated in A by * and

969   **.

970

971

Figure 3-figure supplement 3. Lipid distribution at the subunit cavity. (**A**) Cryo-EM map of Ca^{2+}-bound nhTMEM16 in nanodiscs (grey, contoured at 3.4 σ) with density corresponding to the phospholipid headgroup region of both membrane leaflets in the nanodisc and inside the subunit cavity highlighted in yellow. (**B**) Ribbon representation of the subunit cavity of the Ca^{2+}-bound nhTMEM16 in nanodiscs (grey) with selected sidechains labelled and depicted as sticks. Unassigned density inside the subunit cavity (contoured at 3.9 σ) is shown in yellow. (**C**) Cryo-EM map of Ca^{2+}-free nhTMEM16 in nanodiscs (grey, contoured at 3.4 σ) with density of the

979   phospholipid headgroup region of both membrane leaflets in the nanodisc highlighted in green.

980   No residual density is found at the subunit cavity. A,C The refined and unmasked maps were low-

981   pass filtered to 6 Å.
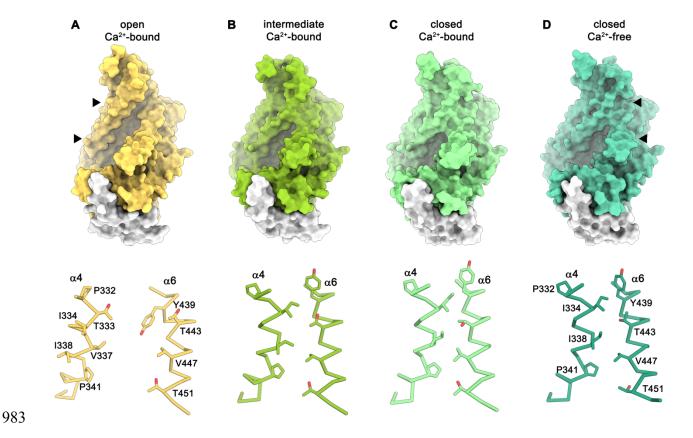
982

983

984   **Figure 4. Conformations of the 'subunit cavity'.** Views of the molecular surface of the subunit

985   cavity (top) and structures of α4 and α6 that line the cavity displayed as Cα-trace with selected

986   sidechains shown as sticks and labeled (bottom). (**A**) 'Open state' as defined in the Ca^{2+}-bound

987   structure in nanodiscs. (**B**) 'Intermediate state' as defined in the Ca^{2+}-bound structure in nanodiscs,

988   (**C**) 'Ca^{2+}-bound closed state' as defined in the Ca^{2+}-bound structure in nanodiscs. (**D**) 'Closed

989   state' as defined by the Ca^{2+}-free structure in nanodiscs. The region shown in the lower panels is

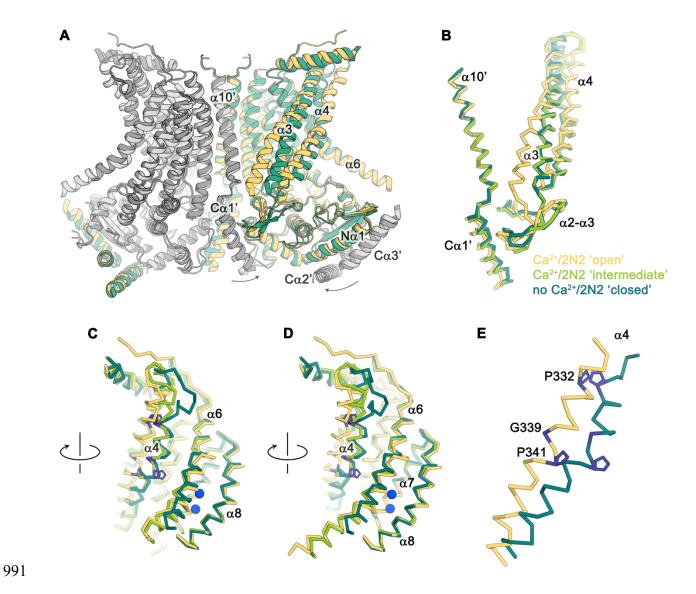990   depicted by triangles in the upper panels.

991

Figure 5. Conformational changes. (**A**) Ribbon representation of a superposition of the Ca^{2+}-bound 'open' (yellow and light grey) and Ca^{2+}-free 'closed' (green and dark grey) nhTMEM16 structures in nanodiscs. Selective helices are labeled and the arrows indicate small rearrangements of the cytosolic domain upon Ca^{2+}-release. (**B-D**) $C\alpha$-traces of selected regions of the 'subunit cavity' in different conformations as defined by the Ca^{2+}-bound 'open' structure in nanodiscs (yellow), the Ca^{2+}-bound 'intermediate' structure in nanodiscs (light green) and the Ca^{2+}-free 'closed' structure in nanodiscs (dark green). The view in B is as in A and the respective orientations

999   of subsequent panels are indicated. (**D**) Superposition of α4 in the 'open' and closed' states with

1000   residues that act as potential pivots for structural arrangements highlighted in blue.
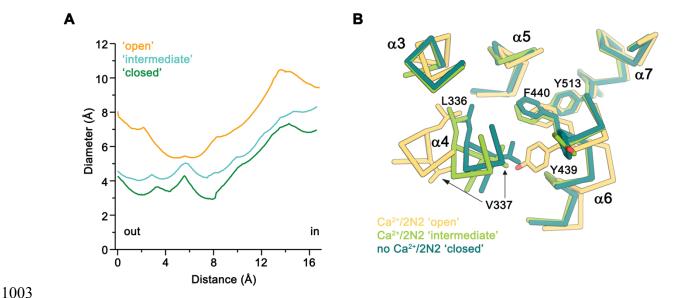
1001

1002

1003

1004   **Figure 5-figure supplement 1. Diameter of the subunit cavity in Ca^{2+}-bound nhTMEM16**

1005   **structures in nanodiscs.** (**A**) Pore diameter at the constriction of the subunit cavity in the three

1006   conformations of the subunit cavity calculated with HOLE (Smart et al., 1996). (**B**) View of the

1007   constriction of the 'subunit cavity' in three different conformations from the extracellular side.

1008   The protein is shown as Cα-trace with selected sidechains displayed as sticks and labelled.
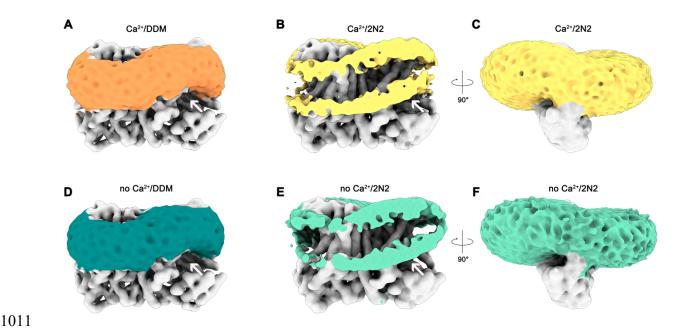
1009

1010

1011

Figure 6. Detergent and lipid interactions. Refined and unmasked cryo-EM density map low-pass filtered to 6 Å are shown. (**A**) Map of the Ca^{2+}-bound nhTMEM16 data in detergent contoured at 4 σ ; (**B**,**C**) Map of the Ca^{2+}-bound nhTMEM16 data in nanodiscs contoured at 3.2 and 1.6 σ; (**D**) Map of the Ca^{2+}-free nhTMEM16 data in detergent contoured at 4 σ; (**E** and **F**), Map of the Ca^{2+}-free nhTMEM16 data in nanodiscs contoured at 3.2 and 1.6 σ. The density corresponding to the detergent micelle or the nanodisc, which is composed of lipids surrounded by the 2N2 belt protein, are colored in orange, yellow, dark green and light green, respectively, density of nhTMEM16 is shown in grey. A,B,D,E show a front view of the dimer similar to Figure 1A and the subunit cavity is indicated by a white arrow. B, E, clipped maps reveal the headgroup regions of both membrane leaflets. C,F, are viewed in direction of the subunit cavity.
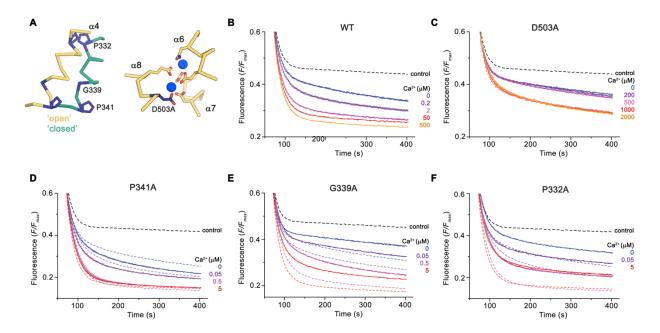
1022

1023

Figure 7. Functional properties of mutants. (**A**) Regions of nhTMEM16 harboring mutated residues. Left, Cα-trace of α4 in 'open' (yellow) and 'closed' (green) conformations of Ca^{2+}-bound nhTMEM16 in nanodiscs. Right, ion binding site with Ca^{2+}-ions shown in blue. (**B-F**) Ca^{2+}-dependence of scrambling activity in nhTMEM16-containing proteoliposomes. Traces depict sections of the fluorescence decrease of tail-labeled NBD-PE lipids after addition of dithionite at different Ca^{2+} concentrations. Data show averages of three technical replicates, errors are s.e.m.. Ca^{2+} concentrations (μM) are indicated. Full traces are displayed in Fig7-figure supplement 1. (B) WT, (C) D503A, (D) P341A, (E) G339A, and (F) P332A. (D to F) The traces of WT reconstituted in the same batch of liposomes are shown as dashed lines in the same color as their corresponding conditions of the mutant for comparison. (B to F), The black dashed line refers to the fluorescence decay in protein-free liposomes.
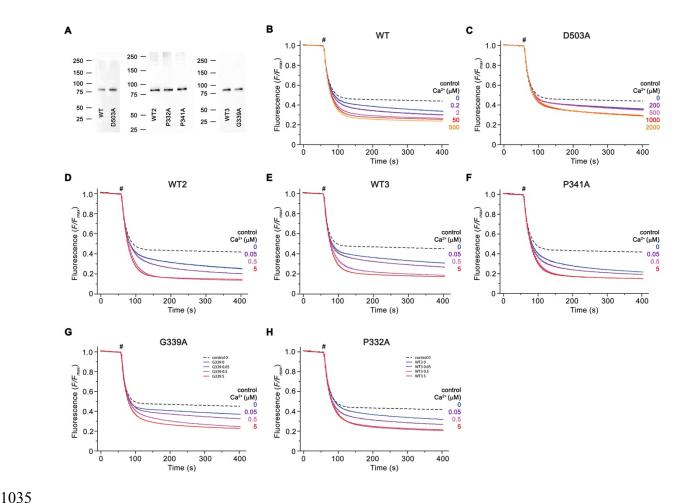
67

1035

Figure 7-figure supplement 1. Reconstitution efficiency. (A) Reconstitution efficiency of nhTMEM16 mutants compared to WT (WT1, WT2, WT3) reconstituted in the same batch of solubilized lipids. For analysis, equivalent amounts of liposomes were loaded on SDS-PAGE and detected with an anti-my antibody detecting a fusion tag on the protein. The positions of molecular weight markers (kDa) are indicated. **(B-H)** Traces of scrambling experiments displayed in Figure 7. Data show averages of three technical replicates, errors are s.e.m.. Ca^{2+}-dependence of scrambling activity of WT1 **(B)** and D503A **(C)** displayed in Figure 7B and C. **(D)** Ca^{2+}-dependence of scrambling activity of WT2 displayed for comparison in Figures 7D and F. **(E)** Ca^{2+}-dependence of scrambling activity of WT3 displayed for comparison in Figure 7E. **(F)** Ca^{2+}-dependence of scrambling activity of P341A displayed for comparison in Figure 7D. **(G)** Ca^{2+}-

1046   dependence of scrambling activity of G339A displayed for comparison in Figure 7E. (**H**) Ca^{2+}-

1047   dependence of scrambling activity of P332A displayed for comparison in Figure 7F. Traces depict

1048   fluorescence decrease of tail-labeled NBD-PE lipids after addition of dithionite (#) at different

1049 Ca^{2+} concentrations. Data show averages of three technical replicates. Ca^{2+} concentrations (µM)
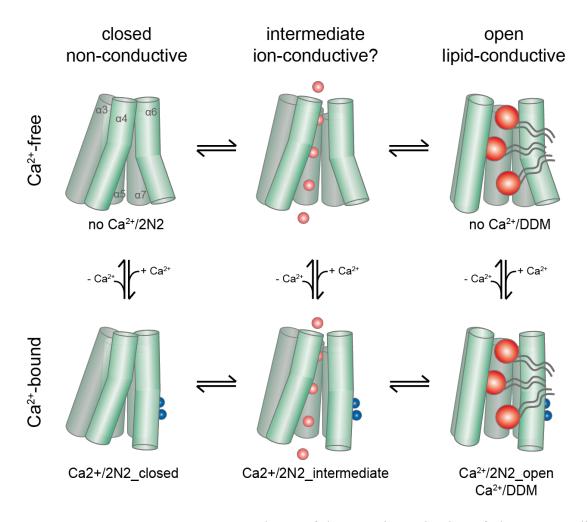
1050   are indicated.

1051

1052

1053   **Figure 8. Activation mechanism.** Scheme of the stepwise activation of nhTMEM16 displaying

1054   the equilibrium of states in Ca^{2+}-bound and Ca^{2+}-free conditions. Conformations obtained in this

1055   study and their correspondence to distinct states are indicated. Ca^{2+} and permeating ions are

1056 depicted as blue and red spheres, respectively. Phospholipid headgroups are shown as red spheres

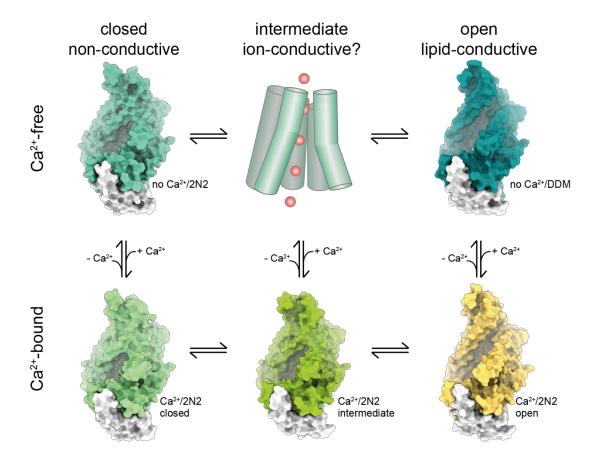1057 and acyl chains as grey tails.

1058

1059

1060 **Figure 8-figure supplement 1. Activation mechanism.** Scheme of the stepwise activation of

1061 nhTMEM16 as shown in Figure 8 with the states displayed by the surface representation of the

1062 respective conformation.

1063

Table 1. Cryo-EM data collection, refinement and validation statistics.

	nhTMEM16, DDM, +Ca^{2+} (EMDB-4588, PDB 6QM5)	nhTMEM16, DDM, -Ca^{2+} (EMDB-4589, PDB 6QM6)	nhTMEM16, 2N2, -Ca^{2+} (EMDB-4587, PDB 6QM4)
Data collection and processing			
Microscope	FEI Talos Arctica	FEI Talos Arctica	FEI Talos Arctica
Camera	Gatan K2 Summit + GIF	Gatan K2 Summit + GIF	Gatan K2 Summit + GIF
Magnification	49,407	49,407	49,407
Voltage (kV)	200	200	200
Exposure time frame/total (s)	0.15/9	0.15/9	0.15/9
Number of frames per image	60	60	60
Electron exposure (e–/Å^2)	52	52	52
Defocus range (μm)	-0.5 to -2.0	-0.5 to -2.0	-0.5 to -2.0
Pixel size (Å)	1.012	1.012	1.012
Box size (pixels)	220	240	240
Symmetry imposed	C2	C2	C2
Initial particle images (no.)	251,693	570,203	1,379,187
Final particle images (no.)	120,086	238,070	133,961
Map resolution (Å)			
0.143 FSC threshold	3.64	3.68	3.79
Map resolution range (Å)	3.4-5.0	3.4-5.0	3.3-5.0
Refinement			
Initial model used	PDB 4WIS	6QM5	6QMB
Model resolution (Å)	3.6	3.7	3.8
FSC threshold			
Model resolution range (Å)	80-3.6	80-3.7	80-3.8
Map sharpening B factor (Å^2)	-126	-147	-150
Model composition			
Nonhydrogen atoms	10874	10852	10578
Protein residues	1346	1344	1308
Ligands	4	-	-
B factors (Å^2)			
Protein	55.75	76.42	94.09
Ligand	33.72	-	-
R.m.s. deviations			
Bond lengths (Å)	0.007	0.004	0.007
Bond angles (°)	0.821	0.835	0.983
Validation			
MolProbity score	1.47	1.42	1.53
Clashscore	4.02	4.35	4.09
Poor rotamers (%)	0	0	0
Ramachandran plot			
Favored (%)	95.92	96.74	95.17
Allowed (%)	4.08	3.26	4.83
Disallowed (%)	0	0	0

1064

1065

71

1066 **Table 2. Cryo-EM data collection, refinement and validation statistics of the Ca²⁺ bound**

1067 **nhTMEM16 in nanodiscs.**

	nhTMEM16, 2N2, +Ca²⁺ open (EMDB-4592, PDB 6QM9)	nhTMEM16, 2N2, +Ca²⁺ intermediate-closed (EMDB-4593, PDB 6QMA)	nhTMEM16, 2N2, +Ca²⁺ closed (EMDB-4594, PDB 6QMB)
Data collection and processing			
Microscope		FEI Talos Arctica	
Camera		Gatan K2 Summit + GIF	
Magnification		49,407	
Voltage (kV)		200	
Exposure time frame/total (s)		0.15/9	
Number of frames per image		60	
Electron exposure (e–/Å²)		52	
Defocus range (μm)		-0.5 to -2.0	
Pixel size (Å)		1.012	
Box size (pixels)		240	
Symmetry imposed		C2	
Initial particle images (no.)		2,440,110	
Final particle images (no.)	71,175	33,310	41,631
Map resolution (Å)			
0.143 FSC threshold	3.57	3.68	3.57
Map resolution range (Å)	3.4 – 5	3.6 – 5	3.4 – 5
Refinement			
Initial model used	6QM5	6QMB	6QM5
Model resolution (Å) FSC threshold	3.6	3.7	3.6
Model resolution range (Å)			
Map sharpening B factor (Å²)	-114	-96	-95
Model composition			
Nonhydrogen atoms	10878	10714	10696
Protein residues	1346	1324	1322
Ligands	4	4	4
B factors (Å²)			
Protein	77.93	84.86	88.53
Ligand	54.34	57.57	67.10
R.m.s. deviations			
Bond lengths (Å)	0.005	0.006	0.008
Bond angles (°)	0.880	0.872	0.858
Validation			
MolProbity score	1.36	1.38	1.42
Clashscore	3.74	4.69	3.90
Poor rotamers (%)	0	0.18	0
Ramachandran plot			
Favored (%)	96.82	97.23	96.38
Allowed (%)	3.18	2.77	3.62
Disallowed (%)	0	0	0

1068   **Video 1. Conformational transitions.** Shown is a morph between distinct conformational states

1069   obtained for nhTMEM16, namely: the Ca^{2+}-bound 'open' state obtained for nhTMEM16 in

1070   nanodiscs; the 'intermediate' state obtained for nhTMEM16 in lipid nanodiscs; the 'closed' state

1071   obtained for nhTMEM16 in lipid nanodiscs; and the Ca^{2+}-free closed state obtained for

1072   nhTMEM16 in lipid nanodiscs. Shown is a view of the subunit cavity as depicted in Figure 3 and

1073   4. Ca^{2+} ions are shown as blue spheres.

1074   **Video 2. Micelle and lipid distortion.** Shown are the cryo-EM density maps of nhTMEM16

1075   obtained in detergent in complex with Ca^{2+} (upper left corner), in detergent in absence of Ca^{2+}

1076   (upper right corner), in lipid nanodiscs in complex with Ca^{2+} (lower left corner) and in lipid

1077   nanodiscs in absence of Ca^{2+} (lower right corner). The surrounding environment corresponding to

1078   the detergent micelle (upper panels) or the lipid nanodiscs (lower panels) are colored respectively,

1079   while the rest of the protein is shown in grey. Refined and unmasked cryo-EM maps were low-

1080   pass filtered to 6 Å. Transmembrane α-helices 4 and 6 are labeled at the end, indicating the position

1081   of the subunit cavity.